SIAM J. IMAGING SCIENCES
Vol. 11, No. 1, pp. 94–128

© 2018 Society for Industrial and Applied Mathematics

A Variational Model for Joint Motion Estimation and Image Reconstruction*

Martin Burger†, Hendrik Dirks†, and Carola-Bibiane Schönlieb‡

Abstract. The aim of this paper is to derive and analyze a variational model for the joint estimation of motion and reconstruction of image sequences, which is based on a time-continuous Eulerian motion model. The model can be set up in terms of the continuity equation or the brightness constancy equation. The analysis in this paper focuses on the latter for robust motion estimation on sequences of two-dimensional images. We rigorously prove the existence of a minimizer in a suitable function space setting. Moreover, we discuss the numerical solution of the model based on primal-dual algorithms and investigate several examples. Finally, the benefits of our model compared to existing techniques, such as sequential image reconstruction and motion estimation, are shown.

Key words. dynamic image reconstruction, motion estimation, image denoising, joint variational model, regularization, Eulerian motion model

AMS subject classifications. 68U10, 65K10, 65M06

DOI. 10.1137/16M1084183

1. Introduction.

Image reconstruction and motion estimation are important tasks in image processing. Such problems arise for example in modern medicine, biology, chemistry, and physics, where even the smallest objects are observed by high resolution microscopes. To characterize the dynamics involved in such data, velocity fields between consecutive image frames are calculated. This is challenging, since the recorded images often suffer from low resolution, low contrast, different gray levels, and noise. Methods that simultaneously denoise the recorded image sequence and calculate the underlying velocity field offer new opportunities, since both tasks may endorse each other.

Our ansatz aims at reconstructing a given sequence u of images and calculating flow fields $\boldsymbol{v}$ between subsequent images at the same time. For given measurements $f = Ku$ this can be

*Received by the editors July 12, 2016; accepted for publication (in revised form) September 12, 2017; published electronically January 11, 2018.

http://www.siam.org/journals/siims/11-1/M108418.html

Funding: This work is based on research that has been done while the second author was at the University of Cambridge supported by a David Crighton Fellowship. This work was supported by ERC via Grant EU FP 7 - ERC Consolidator Grant 615216 LifeInverse. The work of the first author was also supported by the German Science Foundation DFG via EXC 1003 Cells in Motion Cluster of Excellence, Münster, Germany. The work of the third author was supported by the Leverhulme Trust project on Breaking the nonconvexity barrier, EPSRC grant EP/M00483X/1, the EPSRC Center EP/N014588/1, the Cantab Capital Institute for the Mathematics of Information, the CHiPS (Horizon 2020 RISE project grant), and from the Alan Turing Institute.

†Institute for Computational and Applied Mathematics and Cells in Motion Cluster of Excellence, University of Münster, 48149 Münster, Germany (martin.burger@wwu.de, hendrik.dirks@wwu.de).

‡Department of Applied Mathematics and Theoretical Physics (DAMTP), University of Cambridge, Cambridge CB3 0WA, UK (C.B.Schoenlieb@damtp.cam.ac.uk).

Copyright © by SIAM. Unauthorized reproduction of this article is prohibited.

Downloaded 07/11/18 to 131.111.184.102. Redistribution subject to SIAM license or copyright; see http://www.siam.org/journals/ojsa.php

achieved by minimizing the variational model

$$\int_0^T \frac{1}{2}\|Ku(\cdot,t)-f(\cdot,t)\|_2^2+\alpha\mathcal{R}(u(\cdot,t))+\beta\mathcal{S}(\boldsymbol{v}(\cdot,t))dt \quad \text{s.t.} \quad \mathcal{M}(u,\boldsymbol{v})=0 \tag{1.1}$$

with respect to u and $\boldsymbol{v}$ simultaneously. The denoising part is based on the Rudin–Osher–Fatemi (ROF) model [34]. The first part $\|Ku-f\|_2^2$ connects the input data f with the image sequence u via a linear operator K that acts on one single time step t. Depending on the application K may model the cutting out of a subset $\Sigma \subset \Omega$ for inpainting, a subsampling for superresolution, a blur for deconvolution, or a Radon transform for computed tomography. Additional a priori information about the structure of u, respectively, $\boldsymbol{v}$ can be incorporated into each frame via the regularization terms $\mathcal{R}(u(\cdot,t))$ and $\mathcal{S}(\boldsymbol{v}(\cdot,t))$, while their significance is weighted using α and β. Finally, flow field and images are coupled by a constraint $\mathcal{M}(u,\boldsymbol{v})=0$ (e.g., the optical flow (2.1)).

In the last two decades, variational models for image reconstruction have become very popular. One of the most famous models, introduced by Rudin, Osher, and Fatemi in 1992 [34], is the total variation (TV) model, where the authors couple an L^2 data fidelity term with a TV regularization. Data term and regularizer in the ROF model match with the first two terms model (1.1). The TV regularization results in a denoised image with cartoon-like features. This model has also been adapted to image deblurring [45], inpainting [39], superresolution [29, 43], and tomographic reconstruction [36, 26]. We collectively call these image reconstruction models.

Estimating the flow from image sequences has been discussed in the literature for decades. Already in 1981, Horn and Schunck proposed a variational model for flow estimation [25]. This basic model uses the L^2 norm for the optical flow term as well as for the gradient regularizer and became very popular. Aubert, Deriche, and Kornprobst analyzed the L^1 norm for the optical flow constraint [1] in 1999 and demonstrated its advantages towards a quadratic L^2 norm. In 2006, Papenberg et al. [31] introduced the TV regularization, respectively, the differentiable approximation, to the field of flow estimation. An efficient duality-based L^1-TV algorithm for flow estimation was proposed by Zach, Pock, and Bischof in 2007 [47]. Model (1.1) also incorporates a flow estimation problem by the constraint $\mathcal{M}(u,\boldsymbol{v})$ and suitable regularization $\mathcal{S}(\boldsymbol{v}(\cdot,t))$. Despite the fact that the optical flow is estimated between subsequent frames in a complete series of images, we do not incorporate time regularization on the flow fields. The problem of time-coherent optical flow can for example be found in [44].

The topic of joint models for motion estimation and image reconstruction was already discussed by Tomasi and Kanade [42] in 1992. Instead of a variational approach, they used a matrix-based discrete formulation with constraints to the matrix rank to find a proper solution. In 2002, Gilland et al. published a joint variational model for gated cardiac CT [22]. For two images, they formulated a data term, based on the Kullback–Leibler divergence (cf. [13] for details) and incorporated the motion field via quadratic deformation term and regularizer. In the field of optimal control Borzi, Ito, and Kunisch [10] formulated a smooth cost functional for an optimal control problem that incorporates the optical flow formulation with unknown image sequence and motion field with an additional initial value problem for the image sequence.

Copyright © by SIAM. Unauthorized reproduction of this article is prohibited.

Downloaded 07/11/18 to 131.111.184.102. Redistribution subject to SIAM license or copyright; see http://www.siam.org/journals/ojsa.php

Downloaded 07/11/18 to 131.111.184.102. Redistribution subject to SIAM license or copyright; see http://www.siam.org/journals/ojsa.php

Bar et al. proposed a variational framework for joint motion estimation and image deblurring in 2007 [4]. The underlying flow is assumed to be a translation and coupled into a blurring model for the foreground and background. This results in a Mumford–Shah-type functional. Also in 2007, Shen et al. proposed a statistical approach for joint motion estimation, segmentation, and superresolution [38]. The model assumes an affine linear transformation of the segmentation labels to incorporate the dynamics and is solved calculating the MAP solution. Another possible approach was given by Brune in 2010 [13]. The four-dimensional (three-dimensional + time) variational model consists of an L^2 data term for image reconstruction and incorporates the underlying dynamics using a variational term, introduced by Benamou and Brenier [6] and Benamou, Brenier and Guitt [7]. In our model, the constraint $\mathcal{M}(u, \boldsymbol{v})$ connects image sequence u and velocity field $\boldsymbol{v}$. We mention a recent development in [15], which also discusses a joint motion estimation and image reconstruction model in a similar spirit. The focus there is, however, motion compensation in the reconstruction relative to an initial state, consequently a Lagrangian approach with the initial state as reference image is used and the motion is modeled via hyperelastic deformations. Finally, in [8] Benamou, Carlier, and Santambrogio draw a connection to stochastic mean field games, where the underlying motion is described from the Eulerian and Lagrangian perspectives.

1.1. Contents. The paper is structured as follows: In section 2 we briefly introduce a basic framework for variational image reconstruction and motion estimation and combine both which leads to our joint model. Afterwards, we give a detailed proof for the existence of a minimizer based on the fundamental theorem of optimization in section 3. Finally, we introduce a numerical framework for minimizing our model in section 4 and evaluate the proposed model in different image processing applications in section 5.

2. Joint motion estimation and image reconstruction.

2.1. Noise sensitivity of motion estimation. Throughout this work let $\Omega \subset \mathbb{R}^2$ be an image domain and $\Omega_T := \Omega \times [0, T]$ a space-time domain. One of the most common techniques to formally link intensity variations in image sequences $u(x, t)$ to the underlying velocity field $\boldsymbol{v}(x, t)$ is the optical flow constraint. Based on the assumption that the image intensity $u(x, t)$ is constant along a trajectory $x(t)$ with $\frac{dx}{dt} = \boldsymbol{v}(x, t)$ we get, using the chain rule,

$$0 = \frac{du}{dt} = \frac{\partial u}{\partial t} + \sum_{i=1}^{n} \frac{\partial u}{\partial x_i} \frac{dx_i}{dt} = u_t + \nabla u \cdot \boldsymbol{v}. \tag{2.1}$$

The last equation is generally known as the *brightness constancy assumption*. The assumption constitutes in every point $x \in \Omega_T$ one equation, but in the context of motion estimation from images we usually have two or three spatial dimensions. Consequently, the problem is massively underdetermined. However, it is possible to estimate the motion using a variational model

$$\min_{\boldsymbol{v}} \mathcal{D}(u, \boldsymbol{v}) + \alpha \mathcal{R}(\boldsymbol{v}),$$

where $\mathcal{D}(u, \boldsymbol{v})$ represents the so-called *data term* and incorporates the optical flow constraint in a suitable norm. The second part $\mathcal{R}(\boldsymbol{v})$ models additional a priori knowledge on $\boldsymbol{v}$ and is denoted as the *regularizer*. The parameter α regulates between data term and regularizer.

Copyright © by SIAM. Unauthorized reproduction of this article is prohibited.

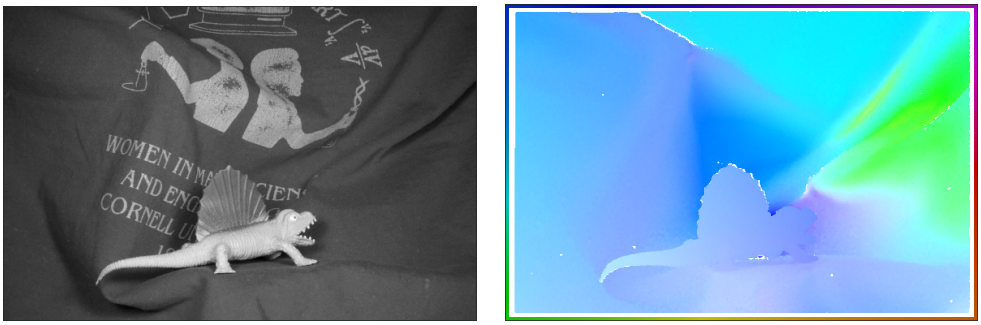

Figure 1. *Image and color-coded ground-truth velocity field from the Middlebury optical flow database* [3].

Possible choices for the data term are

$$\mathcal{D}(u, \boldsymbol{v}) := \frac{1}{2} \|\boldsymbol{v} \cdot \nabla u + u_t\|_2^2 \text{ or } \mathcal{D}(u, \boldsymbol{v}) := \|\boldsymbol{v} \cdot \nabla u + u_t\|_1 .$$

The quadratic L^2 norm can be interpreted as solving the optical flow constraint in a least-squares sense inside the image domain Ω. On the other hand, taking the L^1 norm enforces the optical flow constraint linearly and is able to handle outliers more robustly [1].

The regularizer $\mathcal{R}(\boldsymbol{v})$ has to be chosen such that the a priori knowledge is modeled in a reasonable way. If the solution is expected to be smooth, a quadratic L^2 norm on the gradient of $\boldsymbol{v}$ is chosen as in the classical Horn–Schunck model. Another possible approach is to choose the TV of $\boldsymbol{v}$ if we expect piecewise constant parts of motion, an approach we focus on in this paper.

In practical applications (e.g. microscopy) the recorded images often come with a lack of image quality that is caused by low acquisition times. This leads to another very interesting aspect in motion estimation—how does the noise level on the image data correspond to the quality of the estimated velocity field $\boldsymbol{v}$? To answer this question we created a series of noisy images, where Gaussian noise with increasing variance σ was added. Compare Figure 1 for one of the two images and the corresponding ground-truth velocity field $\boldsymbol{v}_{GT}$. Afterwards, we estimated the motion using the L^1-TV optical flow algorithm. In Figure 2 we plotted the variance of noise on the x-axis versus the *absolute endpoint error* (see (B.1)) of the reconstruction on the y-axis. We observe that already small levels of noise have massive influence on the motion estimation process. Consequently, before estimating the motion field, a preprocessing step may be applied to remove the noise. A more advanced technique is a variational model that is able to simultaneously denoise images and estimate the underlying motion, while both tasks improve each other.

2.2. Proposed model. In the reconstruction process we deal with measured data f, which can be modeled as $f = Ku+\delta$, where δ represents additive noise, often assumed to be Gaussian. The linear operator K represents the forward operator modeling the relation of the image sequence u on the measured data f. This general choice allows us to model applications such as denoising, deblurring, inpainting, super resolution, or even a Radon transform (dynamic CT, PET). Simultaneously we seek the velocity field $\boldsymbol{v} : \Omega_T \to \mathbb{R}^2$ describing the motion in the underlying image sequence u.

Copyright © by SIAM. Unauthorized reproduction of this article is prohibited.

Downloaded 07/11/18 to 131.111.184.102. Redistribution subject to SIAM license or copyright; see http://www.siam.org/journals/ojsa.php

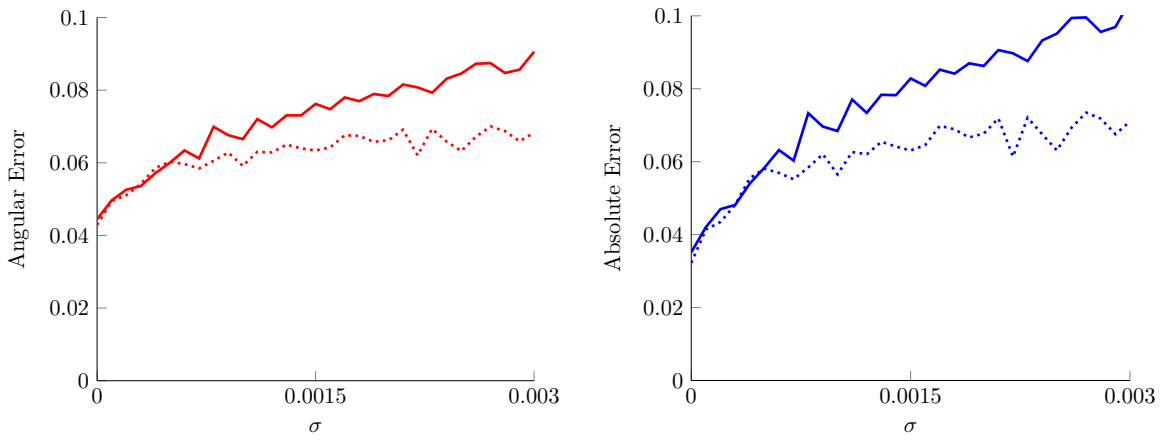

Figure 2. *Angular error (left) and absolute endpoint error (right) for L^1-TV estimated velocity field (solid) and proposed model (dotted) for increasing levels of noise in the underlying data.*

To reconstruct both, u and $\boldsymbol{v}$ at the same time, we propose the following general model:

$$\arg\min_{u,\boldsymbol{v}} \int_0^T \frac{1}{2} \|K_t u(\cdot,t) - f(\cdot,t)\|_2^2 + \alpha \mathcal{R}(u(\cdot,t)) + \beta \mathcal{S}(\boldsymbol{v}(\cdot,t))dt \quad \text{s.t.} \quad \mathcal{M}(u,\boldsymbol{v}) = 0 \quad \text{in } \mathcal{D}'([0,T]\times\Omega). \tag{2.2}$$

The first term in this functional acts as a data fidelity between the measured data f and the objective function u in the case of Gaussian noise. One may think of other data fidelities such as the L^1 distance for salt and pepper noise or the Kullback–Leibler divergence for Poisson noise.

The second term $\mathcal{R}$ in our general model constitutes a regularizer for the image sequence u. We mention that $\mathcal{R}$ only acts on single time steps For reconstructing smooth images, the quadratic L^2 regularization on the gradient can be used, but a more natural regularization in the context of images is the TV, which preserves edges to some extent and favors locally homogeneous intensities. The TV coincides with the seminorm on the space of functions with bounded variation (BV) and we set

$$\mathcal{R}(u(\cdot,t)) = |u(\cdot,t)|_{BV}\,.$$

We mention that of course other higher-order versions of TV (cf. [9, 12]) can be used for the regularization as well, with hardly any changes in the analysis due to the similar topological properties [11]. Regularizers for the velocity field $\boldsymbol{v}$ can be motivated very similarly to those for images. An L^2 penalization of the gradient of $\boldsymbol{v}$,

$$\mathcal{S}(\boldsymbol{v}(\cdot,t)) = \|\nabla \boldsymbol{v}(\cdot,t)\|_2^2\,,$$

leads to smooth velocity fields whereas a TV-based regularizer

$$\mathcal{S}(\boldsymbol{v}(\cdot,t)) = |\boldsymbol{v}(\cdot,t)|_{BV}$$

Downloaded 07/11/18 to 131.111.184.102. Redistribution subject to SIAM license or copyright; see http://www.siam.org/journals/ojsa.php

Copyright © by SIAM. Unauthorized reproduction of this article is prohibited.

Downloaded 07/11/18 to 131.111.184.102. Redistribution subject to SIAM license or copyright; see http://www.siam.org/journals/ojsa.php

favors piecewise constant flow fields. We mention that constraints such as an upper bound on the norm of $\boldsymbol{v}$ can be incorporated into $\mathcal{S}$ by adding the characteristic function of the constraint set.

The final ingredient is to connect image data and the flow field by choosing a suitable constraint $\mathcal{M}(u, \boldsymbol{v})$. Using the brightness constancy assumption leads to the classical optical flow constraint and we set

$$\mathcal{M}(u, \boldsymbol{v}) = u_t + \nabla u \cdot \boldsymbol{v}.$$

Another approach that will not be further discussed within this work is given by the continuity equation

$$\mathcal{M}(u, \boldsymbol{v}) = u_t + \nabla \cdot (u\boldsymbol{v})$$

that arises from the natural assumption that mass keeps constant over time. For an extension to sequences of 3d data, the continuity equation is a much more natural assumption than the optical flow.

Both constraints add a nonlinearity to the model, which leads to difficulties in the analysis arising from the product $\nabla u \cdot \boldsymbol{v}$, respectively, $\nabla \cdot (u\boldsymbol{v})$. Moreover, the model becomes nonconvex and thus challenging from a numerical point of view, because local minimizers can appear. On the other hand the motion constraints and possibly strong regularization of motions provide a framework where motion estimation can enhance the image reconstruction and vice versa. In particular this makes the motion estimation more robust to noise (cf. Figure 2). To simplify our notation, we use abbreviations of our model in the structure [*regularizer* u]-[*regularizer* $\boldsymbol{v}$] [*constraint*] as, e.g., for the [TV]-[TV] [optical flow] model. For the sake of readability we will omit the brackets.

2.3. Preliminaries. In what follows we consider gray valued image data u on a space-time domain $\Omega_T := \Omega \times [0, T] \subset \mathbb{R}^2 \times \mathbb{R}^+, u : \Omega_T \to \mathbb{R}$. The sequence of flow fields will be denoted by $\boldsymbol{v}$ and is defined on Ω_T with Neumann boundary conditions in space, $\boldsymbol{v} : \Omega_T \to \mathbb{R}^2$. We expect finite speeds which gives the useful natural bound

$$\|\boldsymbol{v}\|_\infty \leq c_\infty < \infty \quad \text{a.e. in } \Omega \times [0, T]\,. \tag{2.3}$$

This assumption is reasonable since we have an application to real data (e.g., cell movement, car tracking) in mind.

Besides this, a bound on the divergence of $\boldsymbol{v}$ in some Lebesgue space Θ is later needed in order to prove the existence of a minimizer. From the physical point of view the divergence measures the magnitude of the source or sink of $\boldsymbol{v}$. Consequently, having $\nabla \cdot \boldsymbol{v} \in L^p$ means an overall boundedness of sources and sinks, which is, however, not necessarily pointwise Moreover, for the flow $\boldsymbol{v}$ the divergence is a measure of compressibility. We speak of an incompressible flow if $\nabla \cdot \boldsymbol{v} = 0$, so bounding the divergence means bounding the compressibility of $\boldsymbol{v}$.

Definitions and notations are explained in Appendix A. Moreover, we illustrate error measures for velocity fields and explain the discretization of our model in detail there. Finally, the appendix contains a pseudocode and further results.

Copyright © by SIAM. Unauthorized reproduction of this article is prohibited.

Downloaded 07/11/18 to 131.111.184.102. Redistribution subject to SIAM license or copyright; see http://www.siam.org/journals/ojsa.php

3. Analysis of the variational problem. The most challenging model from an analytical viewpoint is the joint TV-TV optical flow model

$$J(u,\boldsymbol{v}) = \int_0^T \frac{1}{2}\left\|Ku-f\right\|_{\mathcal{F}}^2 + \alpha\left|u(\cdot,t)\right|_{BV}^p + \beta\left|\boldsymbol{v}(\cdot,t)\right|_{BV}^q dt \tag{3.1}$$
$$\text{s.t. } u_t + \nabla u\cdot\boldsymbol{v} = 0 \quad \text{in } \mathcal{D}'(\Omega_T),$$
$$\left\|\boldsymbol{v}\right\|_\infty \le c_\infty, \left\|\nabla\cdot\boldsymbol{v}\right\|_\Theta \le c^*$$

for $p>1$ and $q\ge 1$. For simplicity we restrict ourselves to the TV-TV optical flow model with spatial dimension two here. We refer to [18] for the full analysis including other cases such as the mass preservation constraint and L^2 regularization. We want to mention that our results apply for any convex regularizers $\mathcal{R},\mathcal{S}$ satisfying $\mathcal{R}(u(\cdot,t))\ge|u(\cdot,t)|_{BV}^p$ and $\mathcal{S}(\boldsymbol{v}(\cdot,t))\ge|\boldsymbol{v}(\cdot,t)|_{BV}^q$, such as, e.g., the total generalized variation-functional. We assume $K: L^1(\Omega)\to\mathcal{F}(\Omega)$ to be a bounded linear operator to some Hilbert space $\mathcal{F}(\Omega)$. The operator K operates on single time steps only, however, the analysis can be generalized for time dependent K (cf. comment). Note that due to the embedding of Sobolev spaces $W^{1,s}$ into BV, the results can also be generalized to other gradient regularizations with $s>1$. Finally, we mention that in the case of the continuity equation as a constraint the results can even be obtained under weaker conditions if the continuity equation is considered in a weak form; we refer to [18] for further details.

Note that for the following analysis the bound on the divergence of $\boldsymbol{v}$ is crucial. The chosen bound for $\boldsymbol{v}$ induces a condition on the space Θ for which we will need to assume that

$$\exists s>1, k>2: \quad L^{p^*s}(0,T;L^k(\Omega))^2 \hookrightarrow \Theta \tag{3.2}$$

with p^* being the Hölder conjugate of p.

Our main result in this section is the following.

Theorem 3.1. *Let $\Omega\subset\mathbb{R}^2, p,q>1, \hat{p}=\min\{p,2\}$, $K\mathbf{1}\neq 0$, and (3.2) be satisfied. Then there exists a minimizer of (3.1) in the space*

$$\left\{(u,\boldsymbol{v}) : u\in L^{\hat{p}}(0,T;BV(\Omega)), \boldsymbol{v}\in L^q(0,T;BV(\Omega))^2, \nabla\cdot\boldsymbol{v}\in\Theta\right\}.$$

The proof of Theorem 3.1 is based on an application of weak lower semicontinuity and compactness techniques. It follows from the following three properties established below:

1. Weak-star compactness of sublevel sets (coercivity) is shown in Lemma 3.2,
2. Weak-star lower semicontinuity follows from Lemma 3.3,
3. Closedness of the constraint set via convergence in a distributional sense is the most challenging part and will be proven in Lemma 3.6.

We finally mention that most arguments can be extended in a straightforward way if the operator K also changes with time by assuming appropriate regularity assumptions, e.g., having a linear operator bounded into $L^2(0,T;\mathcal{F})$.

3.1. Coercivity and lower semicontinuity. We mention that coercivity and lower semicontinuity are independent of the constraint.

Lemma 3.2 (coercivity). *Let $\hat{p}=\min\{p,2\}$, $K\mathbf{1}\neq 0$, and $(u,\boldsymbol{v})$ be such that*

$$J(u,\boldsymbol{v})\le\nu, \qquad \left\|\boldsymbol{v}\right\|_\infty\le c_\infty.$$

Copyright © by SIAM. Unauthorized reproduction of this article is prohibited.

Downloaded 07/11/18 to 131.111.184.102. Redistribution subject to SIAM license or copyright; see http://www.siam.org/journals/ojsa.php

Then there exists $c \in \mathbb{R}$ *such that*

$$\|u\|_{L^{\hat{p}}(0,T;BV(\Omega))} \leq c, \quad \|\boldsymbol{v}\|_{L^q(0,T;BV(\Omega))} \leq c,$$

and, consequently, the sublevel set

$$\mathcal{S}_\nu := \{u \in \Omega : J(u, \boldsymbol{v}) \leq \nu\}$$

is not empty and precompact in the weak-star topology of $L^{\hat{p}}(0,T;BV(\Omega)) \times L^q(0,T;BV(\Omega))^2$.

Proof. We begin with the bound for u and have to prove that for arbitrary $u \in L^p(0,T;BV(\Omega))$ with $J(u,\cdot) \leq \nu$ we have

$$\|u\|^{\hat{p}}_{L^{\hat{p}}(0,T;BV(\Omega))} \leq 2^{\hat{p}-1} \left(\int_0^T \|u\|^{\hat{p}}_{L^1(\Omega)} \,\mathrm{d}t + \int_0^T |u|^{\hat{p}}_{BV(\Omega)} \,\mathrm{d}t \right) \leq c. \tag{3.3}$$

To deduce this bound we need to estimate each of the two terms in the last line of the inequality.

Since all three terms in energy (3.1) are positive, from $J(u, \boldsymbol{v}) \leq \nu$ we directly get a bound on each of the three parts. It follows that

$$\|Ku - f\|_{L^2(0,T;L^2(\Omega))} \leq \nu,$$

which naturally implies

$$(Ku(\cdot,t) - f(\cdot,t)) \in L^2(\Omega) \quad \text{a.e. in } [0,T].$$

Consequently, $\|Ku(\cdot,t) - f(\cdot,t)\|_{L^2(\Omega)}$ is bounded almost everywhere in $t \in [0,T]$ and we define

$$c_K(t) := \|Ku(\cdot,t) - f(\cdot,t)\|_{L^2(\Omega)}.$$

We want to emphasize here that $c_K(t)$ gives a constant for every time step $t \in [0,T]$, but the integral $\int_0^T c_K^{\hat{p}} \mathrm{d}t$ is only bounded for $1 < \hat{p} \leq 2$ due to the L^2-regularity in time.

Proceeding now to (3.3) we directly get from $J(u,\cdot) \leq \nu$ that

$$\int_0^T |u|^p_{BV(\Omega)} \,\mathrm{d}t = \int_0^T TV(u)^p \mathrm{d}t \leq \nu.$$

Consequently, the crucial point is to find a bound for $\|u\|_{L^p(0,T;L^1(\Omega))}$. Let $t \in [0,T]$ be an arbitrary time step. First, we deduce a bound for this single time step $\|u(\cdot,t)\|_{L^1(\Omega)}$ and start with a decomposition for u:

$$\bar{u} = \frac{1}{|\Omega|} \int_\Omega u(x,t) \mathrm{d}x, \quad u_0 = u(\cdot,t) - \bar{u}.$$

From this definition it follows directly that u_0 fulfills

$$\int_\Omega u_0 \mathrm{d}x = 0 \quad \text{(mean value zero)},$$

Copyright © by SIAM. Unauthorized reproduction of this article is prohibited.

Downloaded 07/11/18 to 131.111.184.102. Redistribution subject to SIAM license or copyright; see http://www.siam.org/journals/ojsa.php

and $TV(u(\cdot,t)) = TV(u_0) \leq \nu$. Using the Poincaré–Wirtinger inequality [28] we obtain an L^2 bound for u_0:

$$\|u_0\|_{L^2(\Omega)} \leq c_3 TV(u_0) \leq c_3 \nu,$$

where c_1, c_2, and c_3 are positive constants. Moreover, we need a bound for $\|K\bar{u}\|_{L^2(\Omega)}$, which we get by calculating

$$\begin{aligned}
\|K\bar{u}\|_{L^2}^2 - 2\|K\bar{u}\|_{L^2}\left(\|K\|\,\|u_0\|_{L^2} + \|f\|_{L^2}\right) &\leq \|K\bar{u}\|_{L^2}^2 - 2\|Ku_0 - f\|_{L^2}\|K\bar{u}\|_{L^2} \\
&\leq \|Ku_0 - f\|_{L^2}^2 + \|K\bar{u}\|_{L^2}^2 - 2\|Ku_0 - f\|_{L^2}\|K\bar{u}\|_{L^2} \\
&= \left(\|Ku_0 - f\|_{L^2} - \|K\bar{u}\|_{L^2}\right)^2 \leq \|Ku_0 + K\bar{u} - f\|_{L^2}^2 \\
&= \|Ku(\cdot,t) - f(\cdot,t)\|_{L^2}^2 \leq c_K(t)^2.
\end{aligned}$$

Defining $x := \|K\bar{u}\|_{L^2(\Omega)}$, $a := \|K\|\,\|u_0\|_{L^2(\Omega)} + \|f\|_{L^2(\Omega)}$, we get the simple quadratic inequality

$$x^2 - 2xa \leq c_K(t)^2 \tag{3.4}$$

and, furthermore, know

$$0 \leq a \leq \|K\|\,c_3\nu + \|f\|_{L^2(\Omega)} =: c_4.$$

Plugging this into the quadratic inequality (3.4) yields the solution

$$0 \leq x \leq c_4 + \sqrt{\nu + c_4^2} \leq c_4 + c_7(c_K(t) + c_4).$$

The assumption $K\mathbf{1} \neq 0$ leads to an estimate for the operator

$$\begin{aligned}
\|K\bar{u}\|_{L^2(\Omega)} = \left|\frac{1}{|\Omega|}\int_\Omega u\mathrm{d}x\right| \|K\mathbf{1}\|_{L^2(\Omega)} &\leq c_4 + \sqrt{\nu + c_4^2} \\
\Leftrightarrow \left|\frac{1}{|\Omega|}\int_\Omega u\mathrm{d}x\right| &\leq \frac{c_4 + c_7(c_K(t) + c_4)}{\|K\mathbf{1}\|_{L^2(\Omega)}} =: c_5(t).
\end{aligned}$$

We are now able to bound the L^1 norm of a single time step $t \in [0,T]$ by a constant $c_u(t)$ as follows:

$$\begin{aligned}
0 \leq \|u(\cdot,t)\|_{L^1(\Omega)} \leq c_6\|u(\cdot,t)\|_{L^2(\Omega)} &= c_6\left\|u_0 + \frac{1}{|\Omega|}\int_\Omega u(x,t)\mathrm{d}x\right\|_{L^2(\Omega)} \\
\leq c_6\left(\|u_0\|_{L^2(\Omega)} + \left|\frac{1}{|\Omega|}\int_\Omega u(x,t)\mathrm{d}x\right|\right) &\leq c_6\left(c_3\nu + c_5(t)\right) =: c_u(t).
\end{aligned}$$

Since we are integrating over all these constants $c_u(t)$ and the integral is only bounded for $1 < \hat{p} \leq 2$, we see that the assumption on $\hat{p}$ and p is crucial. Consequently, we have

$$\int_0^T \|u(\cdot,t)\|_{L^1(\Omega)}^{\hat{p}}\,\mathrm{d}t \leq \int_0^T c_u(t)^{\hat{p}}\mathrm{d}t \leq c_M.$$

Copyright © by SIAM. Unauthorized reproduction of this article is prohibited.

Downloaded 07/11/18 to 131.111.184.102. Redistribution subject to SIAM license or copyright; see http://www.siam.org/journals/ojsa.php

Combining both estimates we conclude with the required bound for arbitrary $u \in L^{\hat{p}}(0,T;BV(\Omega))$:

$$\|u\|^{\hat{p}}_{L^{\hat{p}}(0,T;BV(\Omega))} = \int_0^T \|u\|^{\hat{p}}_{BV(\Omega)}\,\mathrm{d}t \le \int_0^T \|u\|^{\hat{p}}_{L^1(\Omega)}\,\mathrm{d}t + \int_0^T |u|^{\hat{p}}_{BV(\Omega)}\,\mathrm{d}t \le c_M T + \nu.$$

A bound for $\boldsymbol{v}$ is easier to establish, since we have $\|\boldsymbol{v}\|_{L^\infty(\Omega)} \le c_\infty$ (see (2.3)) almost everywhere. Similar to u, from $J(u,\boldsymbol{v}) \le \nu$ we obtain the a priori bound

$$\int_0^T |\boldsymbol{v}(\cdot,t)|^q_{BV(\Omega)}\,\mathrm{d}t \le \nu$$

for $\boldsymbol{v}$ from (3.1). We calculate the bound for $\boldsymbol{v}$ directly as

$$\begin{aligned}\|\boldsymbol{v}\|^q_{L^q(0,T;BV(\Omega))} &= \int_0^T \|\boldsymbol{v}(\cdot,t)\|^q_{BV(\Omega)}\,\mathrm{d}t \le \int_0^T \|\boldsymbol{v}(\cdot,t)\|^q_{L^1(\Omega)}\,\mathrm{d}t + \int_0^T |\boldsymbol{v}(\cdot,t)|^q_{BV(\Omega)}\,\mathrm{d}t \\ &\le \int_0^T c_{\boldsymbol{v}}^q\,|\Omega|\,\mathrm{d}t + \nu = c_{\boldsymbol{v}}^q\,|\Omega|\,T + \nu,\end{aligned}$$

where we have used the L^∞ bound on $\boldsymbol{v}$. Combining the bounds for u and $\boldsymbol{v}$, we conclude with an application of the Banach–Alaoglu theorem (see, for example, [35]), which yields the required compactness result in the weak-star topology:

It can be shown that $BV(\Omega)$ is the dual space of a Banach space $\mathcal{Y}$ (see [14]). From the duality theory of Bochner spaces (cf. [16]) we get

$$L^{\hat{p}}(0,T;BV(\Omega)) = L^{p^*}(0,T;\mathcal{Y}(\Omega))^*,$$

where p^* is the Hölder conjugate of p. With the same argumentation we get

$$L^q(0,T;BV(\Omega)) = L^{q^*}(0,T;\mathcal{Y}(\Omega))^*.$$

Since both spaces are duals, an application of the Banach–Alaoglu theorem yields the compactness in the weak-star topology. ∎

Lemma 3.3. *The functional J is lower semicontinuous with respect to the weak-star topology of $L^{\hat{p}}(0,T;BV(\Omega)) \times L^q(0,T;BV(\Omega))^2$.*

Proof. Norms and affine norms as well as their powers with an exponent larger than or equal to one are always convex. Convex functionals on Banach spaces can be proven to be weakly lower semicontinuous. Due to the reflexivity of L^2 we directly obtain weak-star lower semicontinuity.

Furthermore, it can be shown [14] that the TV is weak-star lower semicontinuous. This property holds for exponentials p of TV satisfying $p > 1$.

Lower semicontinuity holds for sums of lower semicontinuous functionals, which concludes the proof. ∎

3.2. Convergence of the constraint. For completing the existence proof we have to deduce closedness of the constraint set. Consider admissible sequences u^n and $\boldsymbol{v}^n$ in a sublevel

Copyright © by SIAM. Unauthorized reproduction of this article is prohibited.

Downloaded 07/11/18 to 131.111.184.102. Redistribution subject to SIAM license or copyright; see http://www.siam.org/journals/ojsa.php

set of J. From the regularization we obtain boundedness and consequently weak* convergence

$$u^n \rightharpoonup^* u, \quad \boldsymbol{v}^n \rightharpoonup^* \boldsymbol{v}.$$

In this context, the most challenging point is to prove convergence (in at least a distributional sense) of the constraint

$$(u_t)^n + \nabla u^n \cdot \boldsymbol{v}^n \to u_t + \nabla u \cdot \boldsymbol{v}.$$

The major problem arises from the product $\nabla u^n \cdot \boldsymbol{v}^n$, which does not necessarily converge to the product of their individual limits. A counterexample can be found in [41]. To achieve convergence we need at least one of the factors to converge strongly, but this cannot be deduced from boundedness directly. A way out uses the Aubin–Lions theorem [2, 27, 40] which yields a compact embedding

$$L^p(0,T;\mathcal{X}) \subset\subset L^p(0,T;\mathcal{Y}),$$

and hence strong convergence in $\mathcal{Y}$, if u^n is bounded in $L^p(0,T;\mathcal{X})$ and $(u_t)^n$ is bounded in $L^r(0,T;\mathcal{Z})$ for some r for Banach spaces $\mathcal{X} \subset\subset \mathcal{Y} \hookrightarrow \mathcal{Z}$. Applied to our case we set $\mathcal{X} = BV(\Omega)$ and $\mathcal{Y} = L^r(\Omega)$. For further analysis it is crucial to consider velocities $\boldsymbol{v}$ in the set

$$\mathcal{V} = \left\{ \boldsymbol{v} \in L^\infty(\Omega)^2 : \ \|\boldsymbol{v}\|_\infty \le c_\infty, \|\nabla \cdot \boldsymbol{v}\|_\Theta \le c^* \right\} \tag{3.5}$$

for positive constants c_∞ and c^*.

The first goal is to calculate a bound for $(u_t)^n$ in some Lebesgue space $L^r(0,T;\mathcal{Z})$, which is given by the following lemma.

Lemma 3.4 (bound for u_t). *Let $\Omega \subset \mathbb{R}^2, u \in L^p(0,T;BV(\Omega)), \boldsymbol{v} \in L^q(0,T;BV(\Omega))^2 \cap \mathcal{V}$ such that $u_t + \nabla u \cdot \boldsymbol{v} = 0$.*

Then we have

$$u_t \in L^{\frac{ps}{p+s-1}}\left(0,T;L^{\frac{2k}{k+1}}(\Omega)\right)$$

with uniform bounds.

Proof. Our goal is to show that a sequence u^n (we will omit the lower n in the following), satisfying the optical flow equation, acts as a bounded linear functional in some Bochner space, thus being an element of the corresponding dual space. We write down the weak form of the optical flow equation with some test function φ:

$$\begin{aligned}
\left|\int_0^T \int_\Omega u_t \varphi \mathrm{d}x\mathrm{d}t\right| &= \left|\int_0^T \int_\Omega u \nabla \cdot (\boldsymbol{v}\varphi) \mathrm{d}x\mathrm{d}t\right| \underbrace{\le}_{\text{Hölder}} \int_0^T \left(\int_\Omega u^2 \mathrm{d}x\right)^{\frac{1}{2}} \left(\int_\Omega (\nabla \cdot (\boldsymbol{v}\varphi))^2 \mathrm{d}x\right)^{\frac{1}{2}} \mathrm{d}t \\
&\underbrace{\le}_{\text{Mink.}} \int_0^T \|u\|_{L^2} \left[\left(\int_\Omega (\varphi \nabla \cdot \boldsymbol{v})^2 \mathrm{d}x\right)^{\frac{1}{2}} + \left(\int_\Omega (\boldsymbol{v} \cdot \nabla \varphi)^2 \mathrm{d}x\right)^{\frac{1}{2}}\right] \mathrm{d}t \\
&= \underbrace{\int_0^T \|u\|_{L^2} \left(\int_\Omega (\varphi \nabla \cdot \boldsymbol{v})^2 \mathrm{d}x\right)^{\frac{1}{2}} \mathrm{d}t}_{(i)} + \underbrace{\int_0^T \|u\|_{L^2} \left(\int_\Omega (\boldsymbol{v} \cdot \nabla \varphi)^2 \mathrm{d}x\right)^{\frac{1}{2}} \mathrm{d}t}_{(ii)}.
\end{aligned}$$

Copyright © by SIAM. Unauthorized reproduction of this article is prohibited.

Downloaded 07/11/18 to 131.111.184.102. Redistribution subject to SIAM license or copyright; see http://www.siam.org/journals/ojsa.php

Let us start with an estimate for part (i), which we obtain after three subsequent applications of the Hölder inequality:

$$\int_0^T \|u\|_{L^2} \left(\int_\Omega (\varphi \nabla \cdot \boldsymbol{v})^2 \mathrm{d}x \right)^{\frac{1}{2}} \mathrm{d}t \leq \|u\|_{L^p(0,T;L^2)} \|\nabla \cdot \boldsymbol{v}\|_{L^{p^* s}(0,T;L^{2k})} \|\varphi\|_{L^{p^* s^*}(0,T;L^{2k^*})}$$

for p^* and s as in the statement of the theorem. An estimate for part (ii) follows using Cauchy–Schwarz and Hölder:

$$\int_0^T \|u\|_{L^2} \left(\int_\Omega (\boldsymbol{v} \cdot \nabla \varphi)^2 \mathrm{d}x \right)^{\frac{1}{2}} \mathrm{d}t \leq c_{\boldsymbol{v}} \int_0^T \|u\|_{L^2} \|\varphi\|_{W^{1,2}} \mathrm{d}t \leq c_{\boldsymbol{v}} \|u\|_{L^p(0,T;L^2)} \|\varphi\|_{L^{p^*}(0,T;W^{1,2})}.$$

Combining these estimates we obtain

$$\begin{aligned} \left| \int_0^T \int_\Omega u_t \varphi \mathrm{d}x \mathrm{d}t \right| &\leq \|u\|_{L^p(0,T;L^2)} \|\nabla \cdot \boldsymbol{v}\|_{L^{p^* s}(0,T;L^{2k})} \|\varphi\|_{L^{p^* s^*}(0,T;L^{2k^*})} \\ &\quad + c_{\boldsymbol{v}} \|u\|_{L^p(0,T;L^2)} \|\varphi\|_{L^{p^*}(0,T;W^{1,2})} \\ &\leq (\|\nabla \cdot \boldsymbol{v}\|_{L^{p^* s}(0,T;L^{2k})} + c_{\boldsymbol{v}}) \|u\|_{L^p(0,T;L^2)} \|\varphi\|_{L^{p^* s^*}(0,T;L^{2k^*})}. \end{aligned}$$

In the first inequality, we used the embedding

$$W^{1,2}(\Omega) \hookrightarrow L^{2k^*}(\Omega) \quad \forall 1 \leq k^* < \infty.$$

The sum of the first terms is bounded because of the assumptions made above. A bound for u follows again from the $BV(\Omega)$ embedding into $L^2(\Omega)$ and we conclude

$$\langle u_t, \varphi \rangle := \int_0^T \int_\Omega u_t \varphi \mathrm{d}x \mathrm{d}t \leq C \|\varphi\|_{L^{p^* s^*}(0,T;L^{2k^*})}.$$

Thus, u_t forms a bounded linear functional on $L^{p^* s^*}(0,T;L^{2k^*}(\Omega))$ and we end up with

$$u_t \in \left(L^{p^* s^*}(0,T;L^{2k^*}(\Omega)) \right)^* = L^{\frac{ps}{p+s-1}} \left(0,T;L^{\frac{2k}{k+1}}(\Omega) \right). \qquad \blacksquare$$

Theorem 3.5 (compact embedding for u). *Let $\Omega \subset \mathbb{R}^2$, $\boldsymbol{v} \in L^q(0,T;BV(\Omega))^2 \cap \mathcal{V}$. Then the set*

$$\{u \in L^p(0,T;BV(\Omega)) : \|u\| \leq C, u_t + \nabla u \cdot \boldsymbol{v} = 0\}$$

can be compactly embedded into $L^p(0,T;L^r(\Omega))$ for $\frac{2k}{k+1} \leq r < 2$, and k as in constraint (3.2).

Proof. We have a natural a priori estimate for u in $L^p(0,T;BV(\Omega))$. We moreover deduced a bound for u_t in $L^{\frac{ps}{p+s-1}}(0,T;L^{\frac{2k}{k+1}}(\Omega))$. Embeddings of $BV(\Omega)$ into $\mathcal{Y} = L^r(\Omega)$ are compact for $r < \frac{n}{n-1}$, where n is the spatial dimension. Moreover, the embedding $L^r(\Omega) \hookrightarrow L^{\frac{2k}{k+1}}(\Omega)$ is continuous for $\frac{2k}{k+1} \leq r$. Combining this we see that embedding

$$BV(\Omega) \subset\subset L^r(\Omega) \hookrightarrow L^{\frac{2k}{k+1}}(\Omega)$$

is fulfilled for all $\frac{2k}{k+1} \leq r < 2$. An application of the Aubin–Lions Lemma A.1 yields the compact embedding

$$\{u : u \in L^p(0,T;BV(\Omega)), u_t + \nabla u \cdot \boldsymbol{v} = 0\} \subset\subset L^p(0,T;L^r(\Omega)). \qquad \blacksquare$$

Copyright © by SIAM. Unauthorized reproduction of this article is prohibited.

Downloaded 07/11/18 to 131.111.184.102. Redistribution subject to SIAM license or copyright; see http://www.siam.org/journals/ojsa.php

Another application of this fairly general result can be found in [18]. With this compact embedding result we conclude with strong convergence for $u^n \to u$ in $L^p(0,T;L^r(\Omega))$ and are now able to prove convergence of the product $\nabla u^n \cdot \boldsymbol{v}^n$ to the product of their individual limits $\nabla u \cdot \boldsymbol{v}$.

Lemma 3.6 (convergence of the constraint). *Let $\Omega \subset \mathbb{R}^2, u^n \in L^p(0,T;BV(\Omega))$, and $\boldsymbol{v}^n \in L^q(0,T;BV(\Omega))^2 \cap \mathcal{V}$ be bounded sequences. Then*

$$(u_t)^n + \nabla u^n \cdot \boldsymbol{v}^{\boldsymbol{n}} \rightharpoonup u_t + \nabla u \cdot \boldsymbol{v}$$

in the sense of distributions.

Proof. For the following proof let $\varphi \in C_0^\infty(\Omega), u^n \in L^p(0,T;BV(\Omega))$, and $\boldsymbol{v}^n \in L^q(0,T;BV(\Omega))^2$. For the time derivative we simply calculate

$$\int_0^T \int_\Omega ((u_t)^n - u_t)\,\varphi \mathrm{d}x\mathrm{d}t = -\int_0^T \int_\Omega (u^n - u)\,\varphi_t \mathrm{d}x\mathrm{d}t \to 0.$$

Since test functions are dense in the dual space of u, we directly obtain convergence from the weak convergence $u^n \rightharpoonup u$. For the second part we begin with an analogous argument and estimate

$$\begin{aligned}
&-\int_0^T \int_\Omega (\nabla u^n \cdot \boldsymbol{v}^n - \nabla u \cdot \boldsymbol{v})\,\varphi \mathrm{d}x\mathrm{d}t \\
&\quad = \int_0^T \int_\Omega u^n \nabla \cdot (\varphi \boldsymbol{v}^n) - u \nabla \cdot (\varphi \boldsymbol{v}) \mathrm{d}x\mathrm{d}t \\
&\quad = \underbrace{\int_0^T \int_\Omega (u^n - u) \nabla \cdot (\varphi \boldsymbol{v}^n) \mathrm{d}x\mathrm{d}t}_{(i)} + \underbrace{\int_0^T \int_\Omega u \nabla \cdot (\varphi(\boldsymbol{v}^n - \boldsymbol{v})) \mathrm{d}x\mathrm{d}t}_{(ii)}.
\end{aligned}$$

Part (i) can be estimated as follows:

$$\begin{aligned}
&\int_0^T \int_\Omega (u^n - u) \nabla \cdot (\varphi \boldsymbol{v}^n) \mathrm{d}x\mathrm{d}t \\
&\quad \le \|u^n - u\|_{L^p(0,T;L^r)} \, \|\varphi \nabla \cdot \boldsymbol{v}^n + \boldsymbol{v}^n \cdot \nabla \varphi\|_{L^{p^*}(0,T;L^{r^*})} \\
&\quad \le \|u^n - u\|_{L^p(0,T;L^r(\Omega))} \cdot (\|\varphi \nabla \cdot \boldsymbol{v}^n\|_{L^{p^*}(0,T;L^{r^*}(\Omega))} + \|\boldsymbol{v}^n \cdot \nabla \varphi\|_{L^{p^*}(0,T;L^{r^*}(\Omega))}) \\
&\quad \le \|u^n - u\|_{L^p(0,T;L^r(\Omega))} \\
&\qquad \cdot (\underbrace{\|\varphi\|_{L^{p^* s^*}(0,T;L^{r^*}(\Omega))} \|\nabla \cdot \boldsymbol{v}^n\|_{L^{p^* s}(0,T;L^{r^*}(\Omega))}}_{\text{(i.1)}} + \underbrace{\|\boldsymbol{v}^n \cdot \nabla \varphi\|_{L^{p^*}(0,T;L^{r^*}(\Omega))}}_{\text{(i.2)}}).
\end{aligned}$$

(i.1): φ is a test function and therefore bounded. From the assumptions we also have $\nabla \cdot \boldsymbol{v}^n \in L^{p^* s}(0,T;L^{2k}(\Omega))^2$. Consequently, we have to prove

$$L^{p^* s}(0,T;L^{2k}(\Omega)) \hookrightarrow L^{p^* s^*}(0,T;L^{r^*}(\Omega)).$$

In terms of the embedding theory of Lebesgue spaces we show that $2k \ge r^*$. At this point it is important to keep in mind that r and r^* are Hölder conjugated and the embedding theorem

Copyright © by SIAM. Unauthorized reproduction of this article is prohibited.

Downloaded 07/11/18 to 131.111.184.102. Redistribution subject to SIAM license or copyright; see http://www.siam.org/journals/ojsa.php

for optical flow allows $\frac{2k}{k+1} \leq r < 2$. The condition $2k \geq r^*$, on the other hand, translates to $\frac{2k}{2k-1} \leq r$, which is smaller than 2 for all $k > 1$. By taking $\max(\frac{2k}{k+1}, \frac{2k}{2k-1}) \leq r$ both of our r conditions are satisfied. This yields the required bound for $\nabla \cdot \boldsymbol{v}^n$ in $L^{p^*s^*}(0,T;L^{r^*}(\Omega))$.

(i.2): This part is bounded by a constant due to the boundedness of $\boldsymbol{v}^n$ and the characteristics of φ. Following the arguments for strong convergence of u from above, we conceive that (i) tends to zero.

Estimating part (ii) again requires Lebesgue embedding theory, since

$$\int_0^T \int_\Omega u\nabla \cdot (\varphi\,(v^n - v))\,\mathrm{d}x\mathrm{d}t = \int_0^T \int_\Omega \underbrace{u\varphi\nabla \cdot (v^n - v)}_{\text{(ii.1)}} + \underbrace{u(v^n - v)\cdot\nabla\varphi}_{\text{(ii.2)}}\,\mathrm{d}x\mathrm{d}t.$$

(ii.1): Using Lebesgue embedding theory we show

$$\begin{aligned} L^p(0,T;BV(\Omega)) &\hookrightarrow L^p(0,T;L^{\frac{2k}{2k-1}}(\Omega)) = L^p(0,T;L^{(2k)^*}(\Omega)) \\ &\hookrightarrow L^{\frac{ps}{ps-p+1}}(0,T;L^{(2k)^*}(\Omega)) = L^{(p^*s)^*}(0,T;L^{(2k)^*}(\Omega)). \end{aligned}$$

Consequently, $u \in L^{(p^*s)^*}(0,T;L^{(2k)^*}(\Omega))$, which is the dual of $L^{p^*s}(0,T;L^{2k}(\Omega))$. Due to the weak-star convergence of $\nabla \cdot \boldsymbol{v}^n$ part (ii.1) tends to 0 as $n \to \infty$.

(ii.2): The boundedness of $\boldsymbol{v}$ gives us $\boldsymbol{v} \in L^\infty([0,T]\times\Omega)$ and a priori weak-star convergence. Consequently, we need $u\nabla\varphi \in L^1([0,T]\times\Omega)$. Due to the compact embedding $BV(\Omega) \subset\subset L^1(\Omega)$ and $p > 1$ we get $L^p(0,T;BV(\Omega)) \hookrightarrow L^1(0,T;L^1(\Omega))$. This gives us $u \in L^1([0,T]\times\Omega)$ and since test functions are dense in L^1 we end up with the required $u\nabla\varphi \in L^1([0,T]\times\Omega)$.

Putting all arguments together we end up with convergence of the constraint

$$\begin{aligned} \lim_{k\to\infty}\left|\int_0^T\int_\Omega (\nabla u^n\cdot\boldsymbol{v}^n - \nabla u\cdot\boldsymbol{v})\,\varphi\mathrm{d}x\mathrm{d}t\right| \leq\ & C\lim_{k\to\infty}\|u^n - u\|_{L^p(0,T;L^r)} \\ &+ \lim_{k\to\infty}\left|\int_0^T\int_\Omega u\varphi\nabla\cdot(\boldsymbol{v}^n - \boldsymbol{v})\mathrm{d}x\mathrm{d}t\right| \\ &+ \lim_{k\to\infty}\left|\int_0^T\int_\Omega u(\boldsymbol{v}^n - \boldsymbol{v})\cdot\nabla\varphi\mathrm{d}x\mathrm{d}t\right| = 0. \end{aligned}$$

■

In the numerical part of the paper (section 4), we will reformulate the constrained problem into an unconstrained formulation using an L^1 penalty for the optical flow constraint. In the following lemma we prove convergence of solutions of the unconstrained problem to solutions of the constrained formulation when the penalty weight tends to infinity. Let therefore J_∞ denote the functional in the constrained formulation discussed so far and

$$J_\gamma(u,\boldsymbol{v}) := \int_0^T \frac{1}{2}\|Ku - f\|_2^2 + \alpha\,|u(\cdot,t)|_{BV} + \beta\,|\boldsymbol{v}(\cdot,t)|_{BV} + \gamma\,\|u_t + \nabla u\cdot\boldsymbol{v}\|_1\,\mathrm{d}t, \tag{3.6}$$

an unconstrained formulation of our model using an L^1 penalty term with weight $\gamma > 0$. Further let

$$J_\infty(u,\boldsymbol{v}) := \begin{cases} \int_0^T \frac{1}{2}\|Ku - f\|_2^2 + \alpha\,|u(\cdot,t)|_{BV} + \beta\,|\boldsymbol{v}(\cdot,t)|_{BV}\,\mathrm{d}t & \text{if } u_t + \nabla u\cdot\boldsymbol{v} = 0, \\ +\infty & \text{otherwise.} \end{cases} \tag{3.7}$$

In what follows we consider the minimization of J_γ and J_∞, respectively, in the set $L^p(0,T;BV(\Omega)) \times (L^q(0,T;BV(\Omega))^2 \cap \mathcal{V})$.

Copyright © by SIAM. Unauthorized reproduction of this article is prohibited.

Downloaded 07/11/18 to 131.111.184.102. Redistribution subject to SIAM license or copyright; see http://www.siam.org/journals/ojsa.php

Lemma 3.7. *The functionals J_γ are equicoercive in $L^p(0,T;BV(\Omega))\times(L^q(0,T;BV(\Omega))^2\cap\mathcal{V})$ and Γ-converge to J_∞ on bounded sets in the weak* topology of $L^p(0,T;BV(\Omega)) \times L^q(0,T;BV(\Omega))^2$.*

Proof. The existence of a solution for J_γ can be shown in analogy to the existence proof of the constrained model. Moreover, J_γ are equicoercive since $J_\gamma \geq J_0$.

In order to show Γ-convergence we need to show the lower and upper bound inequalities. The upper bound inequality follows in a straightforward way by choosing the recovering sequence for $(u,\boldsymbol{v})$ to be $(u_\gamma,\boldsymbol{v}_\gamma) = (u,\boldsymbol{v})$. Now, let $(u_\gamma,\boldsymbol{v}_\gamma)$ be a sequence of converging to $(u,\boldsymbol{v})$ in the weak* topology. We distinguish two cases:

- Case 1: if $(u,\boldsymbol{v})$ is admissible, i.e., $u_t + \nabla u\cdot\boldsymbol{v} = 0$, then $J_\infty(u,\boldsymbol{v}) = J_0(u,\boldsymbol{v})$. Due to the lower-semicontinuity of J_0 and the nonnegativity of the penalty term we have that
$$J_0(u,\boldsymbol{v}) \leq \operatorname{liminf} J_0(u_\gamma,\boldsymbol{v}_\gamma) \leq \operatorname{liminf} J_\gamma(u_\gamma,\boldsymbol{v}_\gamma).$$
- Case 2: if $(u,\boldsymbol{v})$ is not admissible, i.e., $u_t + \nabla u\cdot\boldsymbol{v} \neq 0$, then by lower semicontinuity
$$0 < \|u_t + \nabla u\cdot\boldsymbol{v}\| \leq \operatorname{liminf}\|(u_\gamma)_t + \nabla u_\gamma\cdot\boldsymbol{v_\gamma}\|,$$
hence, $\operatorname{liminf}\|(u_\gamma)_t + \nabla u_\gamma\cdot\boldsymbol{v_\gamma}\| = \infty = J_\infty(u,\boldsymbol{v})$. ∎

4. Primal-dual numerical realization. Similarly to the analytical part, we illustrate the numerical realization of the joint TV-TV optical flow model. Numerical schemes for the other models can be derived with only minor changes. We refer to [18] for details. The proposed energy (3.1) is a constrained minimization problem. The constraints on $\boldsymbol{v}$ and $\nabla\cdot\boldsymbol{v}$ are technical assumptions for the analysis of the model, where the bounds can be chosen arbitrarily large. Therefore, we neglect them in the following in the numerical considerations. The common strategy for solving constrained optimization problems with linear constraints (such as $Au = f$ with some linear operator A) is an alternating direction method of multipliers (ADMM) [32] or split Bregman [24] method. Unfortunately, these methods cannot be applied directly in our case due to the nonlinearity of the optical flow constraint $u_t + \nabla u\cdot\boldsymbol{v} = 0$. In Appendix C we discuss a potential way of adjusting the ADMM method to our problem.

Here, we propose a different method that can be justified both from the theoretical and the numerical viewpoint. By introducing an L^1 penalty term for the optical flow constraint with additional weight γ we obtain an unconstrained joint minimization problem

(4.1)
$$\arg\min_{u,\boldsymbol{v}} \int_0^T \frac{1}{2}\|Ku-f\|_2^2 + \alpha\|\nabla u\|_{2,1} + \beta\left(\|\nabla v_1\|_{2,1} + \|\nabla v_2\|_{2,1}\right) + \gamma\|u_t + \nabla u\cdot\boldsymbol{v}\|_1\,\mathrm{d}t.$$

In the problem above, the BV seminorm has been replaced with the discrete isotropic TV defined as
$$\|\nabla u\|_{2,1} := \sum_{i,j}\left|\sqrt{u_x(i,j)^2 + u_y(i,j)^2}\right|.$$

In Lemma 3.7 we have proven that (4.1) converges for $\gamma\to\infty$ to the minimizer of the constrained model and we discuss this strategy from a numerical point of view in section 5.4. Due to the dependence of energy (4.1) on the product of $\nabla u\cdot\boldsymbol{v}$, the energy is nonlinear and

Copyright © by SIAM. Unauthorized reproduction of this article is prohibited.

Downloaded 07/11/18 to 131.111.184.102. Redistribution subject to SIAM license or copyright; see http://www.siam.org/journals/ojsa.php

therefore nonconvex. Moreover the involved L^1 norms are nondifferentiable and we have linear operators acting on u and $\boldsymbol{v}$. Hence, minimizing the energy is numerically challenging.

We propose an alternating minimization technique, switching between minimizing with respect to u and with respect to $\boldsymbol{v}$, while fixing the other variable. This leads to the following two-step scheme:

$$u^{k+1} = \arg\min_u \int_0^T \frac{1}{2} \|Ku - f\|_2^2 + \alpha \|\nabla u\|_{2,1} + \gamma \left\| u_t + \nabla u \cdot \boldsymbol{v}^k \right\|_1 \mathrm{d}t, \tag{4.2}$$

$$\boldsymbol{v}^{k+1} = \arg\min_{\boldsymbol{v}} \int_0^T \left\| u_t^{k+1} + \nabla u^{k+1} \cdot \boldsymbol{v} \right\|_1 + \frac{\beta}{\gamma} \left(\|\nabla v_1\|_{2,1} + \|\nabla v_2\|_{2,1} \right) \mathrm{d}t, \tag{4.3}$$

where each of the subproblems is now convex and a primal-dual algorithm [17, 33] can be applied.

Problem in u. Illustrating the problem in u, we have to solve a classical ROF problem [34] coupled with an additional transport term arising from the optical flow component. Each of the terms contains an operator and is therefore dualized. We set

$$F(Cu) := \int_0^T \frac{1}{2} \|Ku - f\|_2^2 + \alpha \|\nabla u\|_{2,1} + \gamma \left\| \left(D_t + v_1^k D_x + v_2^k D_y \right) u \right\|_1 \mathrm{d}t$$

with an underlying operator

$$Cu = \begin{pmatrix} K \\ \nabla \\ D_t + v_1^k D_x + v_2^k D_y \end{pmatrix} u.$$

We first write down the convex conjugate F^* corresponding to F:

$$F^*(\boldsymbol{y}) = \int_0^T \frac{1}{2} \|y_1\|_2^2 + \langle y_1, f \rangle + \delta_{\{y : \|y\|_{2,\infty} \le 1\}}(y_2/\alpha) + \delta_{\{y : \|y\|_\infty \le 1\}}(y_3/\gamma) \mathrm{d}t.$$

We refer to Appendix D for a detailed notation and derivation of the convex conjugates. This leads to the primal-dual problem

$$\arg\min_u \arg\max_{\boldsymbol{y}} \int_0^T \langle Cu, \boldsymbol{y} \rangle - \frac{1}{2} \|y_1\|_2^2 - \langle y_1, f \rangle - \delta_{\{y : \|y\|_{2,\infty} \le 1\}}(y_2/\alpha) - \delta_{\{y : \|y\|_\infty \le 1\}}(y_3/\gamma) \mathrm{d}t.$$

Plugging this into the primal-dual algorithm yields the following iterative systems consisting mostly of proximity problems

$$\begin{aligned}
\tilde{\boldsymbol{y}}^{l+1} &= \boldsymbol{y}^l + \sigma C \left(2u^l - u^{l-1} \right), \\
y_1^{l+1} &= \arg\min_y \left\{ \int_0^T \frac{1}{2} \left\| y - \tilde{y_1}^{l+1} \right\|_2^2 + \frac{\sigma}{2} \|y\|_2^2 + \sigma \langle y, f \rangle \mathrm{d}t \right\}, \\
y_2^{l+1} &= \arg\min_y \left\{ \int_0^T \frac{1}{2} \left\| y - \tilde{y_2}^{l+1} \right\|_2^2 + \delta_{\{y : \|y\|_{2,\infty} \le 1\}}(y/\alpha) \mathrm{d}t \right\}, \\
y_3^{l+1} &= \arg\min_y \left\{ \int_0^T \frac{1}{2} \left\| y - \tilde{y_3}^{l+1} \right\|_2^2 + \delta_{\{y : \|y\|_\infty \le 1\}}(y/\gamma) \mathrm{d}t \right\}, \\
u^{l+1} &= \arg\min_u \left\{ \int_0^T \frac{1}{2} \left\| u - \left(u^l - \tau C^T \boldsymbol{y}^{l+1} \right) \right\|_2^2 \mathrm{d}t \right\}.
\end{aligned}$$

Copyright © by SIAM. Unauthorized reproduction of this article is prohibited.

Downloaded 07/11/18 to 131.111.184.102. Redistribution subject to SIAM license or copyright; see http://www.siam.org/journals/ojsa.php

The parameters σ, τ refer to step sizes. The have to fulfill $\tau\sigma\|C\| \leq 1$ and can be chosen in analogy to [17]. The subproblem for y_1 is a linear L^2 problem which has a direct solution. Both problems for y_2 and y_3 can be solved by projecting pointwise onto the unit ball with radius α, respectively, γ. This leads to the iterative scheme

$$\begin{aligned}
\tilde{\boldsymbol{y}}^{l+1} &= \boldsymbol{y}^l + \sigma C\left(2u^l - u^{l-1}\right),\\
y_1^{l+1} &= \frac{\tilde{y}_1^{l+1} - \sigma f}{\sigma + 1}, y_2^{l+1} = \pi_\alpha\left(\tilde{y_2}^{l+1}\right), y_3^{l+1} = \pi_\gamma\left(\tilde{y_3}^{l+1}\right),\\
u^{l+1} &= u^l - \tau C^T \boldsymbol{y}^{l+1}.
\end{aligned}$$

The projection onto the unit ball is given by

$$\pi_\alpha(y) = \frac{y}{\max(1, \frac{\|y\|_2}{\alpha})}.$$

Problem in $\boldsymbol{v}$. The problem in $\boldsymbol{v}$ is a simple L^1-TV optical flow problem. As a first step, we define $\lambda := \frac{\beta}{\gamma}$ and split out the regularizer in analogy to the problem for u. This leads to the primal-dual formulation of the problem

$$\arg\min_{\boldsymbol{v}} \arg\max_{\boldsymbol{y}} \left\|u_t^{k+1} + \nabla u^{k+1} \cdot \boldsymbol{v}\right\|_1 + \langle C\boldsymbol{v}, \boldsymbol{y}\rangle - \delta_{\{y:\|y\|_{2,\infty}\leq 1\}}\left(\frac{y_1}{\lambda}\right) - \delta_{\{y:\|y\|_{2,\infty}\leq 1\}}\left(\frac{y_2}{\lambda}\right),$$

where $C\boldsymbol{v} := \left(\begin{smallmatrix} \nabla & 0 \\ 0 & \nabla \end{smallmatrix}\right)\boldsymbol{v}$.

Plugging this into the primal-dual algorithm yields the following problems:

$$\begin{aligned}
\tilde{\boldsymbol{y}}^{l+1} &= \boldsymbol{y}^l + \sigma C\left(2\boldsymbol{v}^l - \boldsymbol{v}^{l-1}\right),\\
y_1^{l+1} &= \arg\min_y \left\{\frac{1}{2}\|y - \tilde{y}_1\|_2^2 + \delta_{\{y:\|y\|_{2,\infty}\leq 1\}}\left(\frac{y}{\lambda}\right)\right\},\\
y_2^{l+1} &= \arg\min_y \left\{\frac{1}{2}\|y - \tilde{y}_2\|_2^2 + \delta_{\{y:\|y\|_{2,\infty}\leq 1\}}\left(\frac{y}{\lambda}\right)\right\},\\
\boldsymbol{v}^{l+1} &= \arg\min_{\boldsymbol{v}} \left\{\frac{1}{2}\left\|\boldsymbol{v} - \left(\boldsymbol{v}^k + \tau C^T \boldsymbol{y}^{l+1}\right)\right\|_2^2 + \tau\left\|u_t^{k+1} + \nabla u^{k+1}\cdot\boldsymbol{v}\right\|_1\right\}.
\end{aligned}$$

Similarly to u, the subproblem for $\boldsymbol{y}$ can be solved by pointwise projections onto the L^2 unit ball with radius λ. The proximal problem in $\boldsymbol{v}$ can be directly solved by an affine linear shrinkage formula. Therefore, we set

$$\rho(\boldsymbol{v}) := u_t^{k+1} + \nabla u^{k+1}\cdot\boldsymbol{v}, \quad \boldsymbol{\beta} := \left(u_x^{k+1}, u_y^{k+1}\right).$$

Then the solution is given by

$$\boldsymbol{v} = \tilde{\boldsymbol{v}}^{l+1} + \begin{cases} \tau\boldsymbol{\beta} & \text{if } \rho\left(\tilde{\boldsymbol{v}}^{l+1}\right) < -\tau\|\boldsymbol{\beta}\|_2^2,\\ -\tau\boldsymbol{\beta} & \text{if } \rho\left(\tilde{\boldsymbol{v}}^{l+1}\right) > \tau\|\boldsymbol{\beta}\|_2^2,\\ -\frac{\rho(\tilde{\boldsymbol{v}}^{l+1})}{\|\boldsymbol{\beta}\|_2^2}\boldsymbol{\beta} & \text{else.}\end{cases}$$

Copyright © by SIAM. Unauthorized reproduction of this article is prohibited.

Downloaded 07/11/18 to 131.111.184.102. Redistribution subject to SIAM license or copyright; see http://www.siam.org/journals/ojsa.php

Combining both formulas we obtain the following scheme:

$$\begin{aligned}
\boldsymbol{y}^{l+1} &= \pi_\lambda\left(\boldsymbol{y}^l + \sigma C\left(2\boldsymbol{v}^l - \boldsymbol{v}^{l-1}\right)\right),\\
\tilde{\boldsymbol{v}}^{l+1} &= \boldsymbol{v}^l - \tau C^T \boldsymbol{y}^{l+1},\\
\boldsymbol{v}^{l+1} &= \tilde{\boldsymbol{v}}^{l+1} + \begin{cases} \tau\boldsymbol{\beta} & \text{if } \rho\left(\tilde{\boldsymbol{v}}^{l+1}\right) < -\tau\left\|\boldsymbol{\beta}\right\|_2^2,\\ -\tau\boldsymbol{\beta} & \text{if } \rho\left(\tilde{\boldsymbol{v}}^{l+1}\right) > \tau\left\|\boldsymbol{\beta}\right\|_2^2,\\ -\frac{\rho(\tilde{\boldsymbol{v}}^{l+1})}{\left\|\boldsymbol{\beta}\right\|_2^2}\boldsymbol{\beta} & \text{else.}\end{cases}
\end{aligned}$$

4.1. Discretization. For the spatial regularization parts $\|\nabla u\|_{2,1}$ and $\|\nabla \boldsymbol{v}\|_{2,1}$ we use forward differences to discretize the involved gradient, respectively, backward differences for the adjoint. The coupling term $\|u_t + \nabla_x u \cdot \boldsymbol{v}\|_1$ is the more challenging part. Using forward differences for the time derivative u_t and central differences for the spatial derivatives ∇u yields a stable discretization of the transport equation, because the scheme is solved implicitly. Details can be found in Appendix D.

As a stopping criterion for both minimization subproblems we use the primal-dual residual (see [23]) as a stopping criterion. For the alternating minimization we measure the difference between two subsequent iterations k and $k+1$ by

$$err_{main} := \frac{\left|u^k - u^{k+1}\right| + \left|\boldsymbol{v}^k - \boldsymbol{v}^{k+1}\right|}{2\left|\Omega\right|}$$

and stop if this difference falls below a threshold ϵ. A pseudocode can be found in Appendix E.

5. Numerical evaluation. The proposed main algorithm is implemented in MATLAB. For the subproblems in u and $\boldsymbol{v}$ we use the optimization toolbox FlexBox [19]. The toolbox comes with a C^{++} module, which greatly enhances the runtime. Code and toolbox and be downloaded [19]. In the following evaluation, the stopping criterion was chosen as $\epsilon = \epsilon_u = \epsilon_v = 10^{-6}$. Furthermore, the weighting parameter γ for the optical flow constraint in the joint model is set to 1 in all experiments, which is enough for practical applications (see Table 1). The evaluated parameter range for α is the interval $[0.01, 0.05]$, whereas β takes values in $[0.05, 0.1]$.

5.1. Joint reconstruction and optical flow model versus pure optical flow. In our initial motivation example in Figure 2 in section 2.1 we compare our joint TV-TV optical flow model with the TV-L^1 optical flow model on the Dimetrodon sequence from [3] with increasing levels of noise. We use additive Gaussian noise with variance $\sigma \in [0, 0.03]$. For the pure optical flow model the parameter ranges in $[0, 0.2]$. Both plots from Figure 2 indicate that our joint approach outperformes the pure optical flow model especially at higher noise levels.

5.2. Denoising and motion estimation. To demonstrate the benefits of our model we compare the TV-TV optical flow model with different classical methods for image denoising and motion estimation, on different datasets. For image denoising we compare our joint model with a standard two-dimensional (2d) ROF model [34] and with a modified 2d+t ROF model from [37], which contains an additional time regularization $\|u_t\|_1$ for the image sequence. Both regularizers are equally weighted. For motion estimation purposes we calculate the motion

Copyright © by SIAM. Unauthorized reproduction of this article is prohibited.

Table 1

Energies for the L^1 optical flow penalty term $\|\bar{\boldsymbol{v}} \cdot \nabla \bar{u} + \bar{u}_t\|_1$ and scaled with the L^1 norm u $\frac{\|\bar{\boldsymbol{v}} \cdot \nabla \bar{u} + \bar{u}_t\|_1}{\|\bar{u}\|_1}$ for the evaluated datasets from section 5.2.

γ	Dimetrodon		Grove 2		Hydrangea		Rubber whale		Urban 2	
0.01	1.12e-02	2.26e-02	1.36e-02	2.82e-02	1.20e-02	2.31e-02	1.19e-02	2.19e-02	1.04e-02	2.80e-02
0.1	1.03e-03	1.91e-03	2.03e-03	4.14e-03	1.16e-03	1.96e-03	1.11e-03	1.98e-03	8.82e-04	2.11e-03
1	3.05e-04	5.41e-04	7.99e-04	1.73e-03	1.55e-04	2.21e-04	1.32e-04	2.39e-04	1.78e-04	4.48e-04

field with a TV-L^1 optical flow approach for noisy and for previously TV-denoised image sequences.

Due to the limitations of our model to movements of small magnitude that arise from the first-order Taylor expansion, we take datasets from the Middlebury optical flow database [3] and scale down the available ground-truth flow to a maximum magnitude of 1. Afterwards, these downscaled flows are used to create sequences of images by cubic interpolation of $I_1(x + k\boldsymbol{v})$ (k represents the kth consecutive image). The image sequence is then corrupted with Gaussian noise with variance $\sigma = 0.002$. The weights for each algorithm are manually chosen to obtain the corresponding best results.

Table 2 contains the evaluation results. It becomes clear that our model outperforms both the standard method for image denoising as well as the method for motion estimation significantly. The visualized results can be found in Figure 3. The images suggest good denoising properties while the estimated motion field contains some significant errors which may arise from the noise in the input images. In general, higher regularization parameters for the flow field generate a better structural similarity index (SSIM)/average endpoint error (AEE) ratio. Consequently, the resulting motion fields are dominated by a few constantly moving regions. For example the Dimetrodon sequence (first row in Figure 3) is well approximated by motion in one main direction, except for a few small outliers that occur due to the L^1 optical flow constraint. For datasets that have many objects moving towards different directions, the motion field contains more regions of constant direction. Artifacts appear especially at the boundaries of moving objects, as for example in the Hydrangea and City dataset (third and fifth row in Figure 3). The denoised images, nevertheless, appear visually pleasing. In contrast to standard TV regularization finer details are also visible as, for example, the small tree in the Grove sequence or the structure of the curtains in the rubber whale dataset.

5.3. Temporal inpainting. The proposed model can be adjusted to perform temporal inpainting. Therefore, the data fidelity term $\|Ku - f\|_2^2$ is evaluated only on known frames and the weight α for the total variation is set to zero for unknown frames. A proof of concept is shown in Figure 4, where we chose two known frames as start and end position of the block and let our model interpolate 60 frames in-between given the flow field $\boldsymbol{v}$. As a comparison, the linear interpolation between both images is shown as well. Our model transports the block from top to bottom smoothly, while the linear interpolation fades out the top block, fades in the bottom block, and keeps the middle part constant.

As a real data application we choose the Hamburg taxi sequence from Nagel and the Mini Cooper sequence from the Middlebury database. Both image sequences have an underlying motion with a magnitude larger than one pixel. The model can be adjusted to this situation

Copyright © by SIAM. Unauthorized reproduction of this article is prohibited.

Downloaded 07/11/18 to 131.111.184.102. Redistribution subject to SIAM license or copyright; see http://www.siam.org/journals/ojsa.php

Downloaded 07/11/18 to 131.111.184.102. Redistribution subject to SIAM license or copyright; see http://www.siam.org/journals/ojsa.php

Table 2

Table comparing the joint motion estimation and image reconstruction model with classical models for image denoising and motion estimation. ROF 2D: *Rudin–Osher–Fatemi model applied to single frames of the image sequence;* ROF 2 D+t: *ROF model with additional time-regularization;* OF Noisy: *TV-L^1 optical flow model applied to noisy images;* OF Denoised: *TV-L^1 optical flow model applied to previously TV-denoised images. Previously undefined heading abbreviations are peak signal-to-noise ratio (PSNR) and angular error (AE).*

Dataset	Algorithm	SSIM	PSNR	AEE	AE
Dimetrodon	optical flow noisy	-	-	0.253	0.164
	ROF_{2D} & optical flow	0.86621	79.3403	0.066	0.044
	BM3D & optical flow	0.89688	80.5991	0.071	0.047
	VBM3D & optical flow	**0.924**	**82.693**	0.067	0.045
	our joint model	0.917	82.436	**0.061**	**0.041**
Grove 2	optical flow noisy	-	-	0.298	0.189
	ROF_{2D} & optical flow	0.734	74.454	0.090	0.060
	BM3D & optical flow	0.792	75.551	0.089	0.059
	VBM3D & optical flow	**0.853**	77.667	0.081	0.053
	our joint model	0.851	**78.030**	**0.069**	**0.046**
Hydrangea	optical flow noisy	-	-	0.261	0.167
	ROF_{2D} & optical flow	0.803	76.754	0.085	0.056
	BM3D & optical flow	0.839	77.889	0.071	0.047
	VBM3D & optical flow	0.869	79.952	0.067	0.045
	our joint model	**0.871**	**80.170**	**0.067**	**0.044**
Rubber whale	optical flow noisy	-	-	0.255	0.164
	ROF_{2D} & optical flow	0.777	77.733	0.091	0.061
	BM3D & optical flow	0.810	79.173	0.091	0.061
	VBM3D & optical flow	0.834	**80.539**	0.066	0.044
	our joint model	**0.847**	80.478	**0.065**	**0.043**
Urban 2	optical flow noisy	-	-	0.228	0.148
	ROF_{2D} & optical flow	0.768	78.211	0.094	0.062
	BM3D & optical flow	0.823	79.881	0.086	0.057
	VBM3D & optical flow	**0.851**	**81.147**	0.080	0.053
	our joint model	0.842	80.869	**0.080**	**0.053**

by adding additional frames between the known images and using the model to perform temporal inpainting. The resulting images, time interpolants, and velocity fields are visualized in Figure 5. We zoom into the image to make differences between original and reconstruction better visible. The complete images can be found in Appendix E (Figures 8 and 9). In terms of denoising, both the car in front and the background are more homogeneous. Moreover, the model generated two time interpolants and estimated the flow on the whole sequence.

5.4. Constrained optical flow. Instead of directly minimizing the analytical model, we chose an L^1 penalty term for the optical flow constraint. From the practical perspective, the ADMM [32] or split Bregman [24] method could be applied to the analytical model, but this would lead in both cases to a variational subproblem with an L^2 penalty for the optical flow constraint (see Appendix C). Similarly to our approach, the problem is nonlinear and nonconvex and could be treated in an alternating manner leading to a slightly modified iterative scheme. However, this would increase the numerical complexity due to the fact that the nonlinear problem has to be treated in each iteration of the split Bregman or augmented La-

Copyright © by SIAM. Unauthorized reproduction of this article is prohibited.

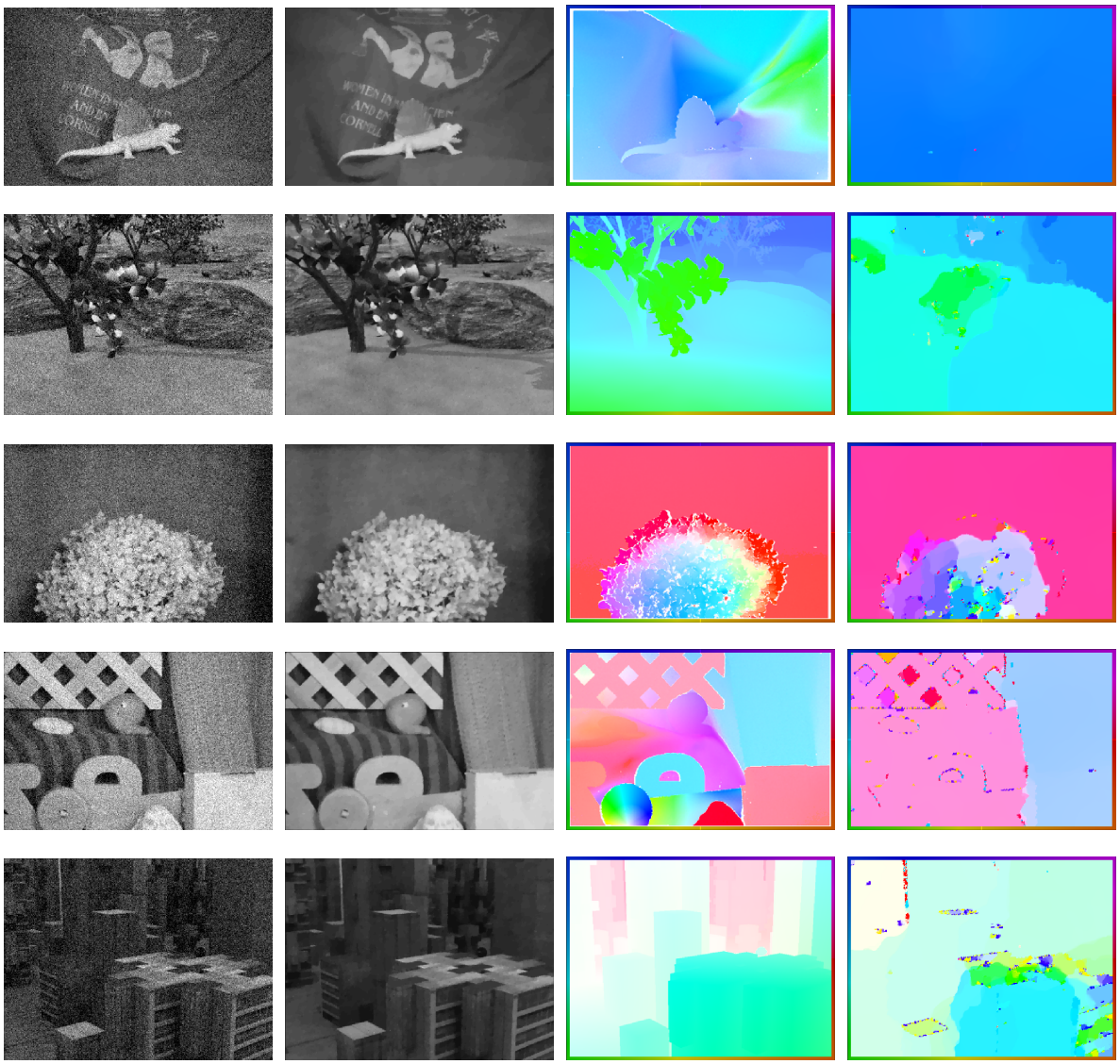

Figure 3. *Image sequences that were generated using data from the Middlebury database* [3]. *Noisy input image and corresponding reconstruction are shown in the first two columns. Ground-truth velocity field and estimated velocity field are shown in columns three and four. The figure contains the second image for each sequence from Table* 2.

grangian method, opposed to our framework which requires the solution of only one nonlinear and nonconvex problem in the L^1 penalty.

From the theoretical side, the choice of an L^1 penalty is justified in Lemma 3.7, where we show that an L^1 penalty is solved exactly for large weighting factors. We evaluate this result numerically using Table 1 in which we denoted the energy of the optical flow constraint $\|\bar{\boldsymbol{v}} \cdot \nabla \bar{u} + \bar{u}_t\|_1$, where $(\bar{u}, \bar{\boldsymbol{v}})$ denotes the minimizer of each dataset from section 5.2.

Copyright © by SIAM. Unauthorized reproduction of this article is prohibited.

Downloaded 07/11/18 to 131.111.184.102. Redistribution subject to SIAM license or copyright; see http://www.siam.org/journals/ojsa.php

(a) (b) (c) (d)

Figure 4. *Temporal inpainting example. For our model, images* (a) *and* (b) *are taken as known input data and the model interpolates* 60 *frames using the optical flow approach. Image* (c) *contains frame* 30 *of the result. As a comparison, the linear interpolation between frame* (a) *and* (b) *is shown in image* (d).

5.5. Image sequences with large-scale motion. Due to the linearization of the optical flow constraint, our model is limited to flows of small magnitude (usually up to one pixel). To better understand the consequences of violating this assumption, we took the original Grove 2 sequence from the Middlebury database which has in total eight images and added Gaussian noise ($\sigma = 0.01$). The ground-truth flow is only available between frame four and five and contains flows up to a magnitude of 5 pixels. First, we applied our classical model with $\alpha = 0.05, \beta = 0.5$, and $\gamma = 1$ to the sequence. The resulting images and flow fields can be found in Figure 6. From a visual point of view, the estimated images look very blurry while moving objects are visible in the colored flow fields but do not have the correct orientation. Due to the time discretization using the difference $u^{i+1} - u^i$, the model calculated flow fields with a maximum magnitude of 2 pixels. Therefore, from the image reconstruction perspective, the optical flow term $\|u^{i+1} - u^i + \nabla u^{i+1} \cdot \boldsymbol{v}^i\|$ compares points in u^i and u^{i+1} that do not match, leading to the blurry result. Next, we used the idea of time interpolation from section 5.3 to address the drawbacks of the standard model. The temporal resolution is enhanced and therefore the motion between consecutive images is reduced. The results can be found in rows four and five in Figure 6. The images look less blurry and the velocity fields are already pointing towards the correct direction.

A third possible approach is given by reducing the spatial resolution of the images and therefore lowering the magnitude of motion. This approach leads to well-known coarse-to-fine optical flow approaches (see, e.g., [31]). Figure 6 also contains results of a modified large-scale framework (see [20]) that is able to handle large-scale motion fields. For the large-scale framework, an explicit time discretization is chosen and the following energy is minimized:

$$\underset{\substack{u=u^1,\dots,u^n \\ \boldsymbol{v}=\boldsymbol{v}^1,\dots\boldsymbol{v}^{n-1}}}{\arg\min} \sum_{i=1}^{n} \frac{1}{2}\|A^i u^i - f^i\|_2^2 + \alpha \left\|\nabla u^i\right\|_{1,2} + \sum_{i=1}^{n-1} \|u^{i+1}(x+\boldsymbol{v}^i) - u^i\|_1 + \beta \sum_{j=1}^{2} \left\|\nabla v^{i,j}\right\|_{1,2}. \tag{5.1}$$

Similarly to modern optical flow approaches, the flow problem is solved on coarser grids first and then iteratively refined. This large-scale framework is formalized in a time-discrete sense and is therefore less amenable to an analytic investigation.

Copyright © by SIAM. Unauthorized reproduction of this article is prohibited.

Downloaded 07/11/18 to 131.111.184.102. Redistribution subject to SIAM license or copyright; see http://www.siam.org/journals/ojsa.php

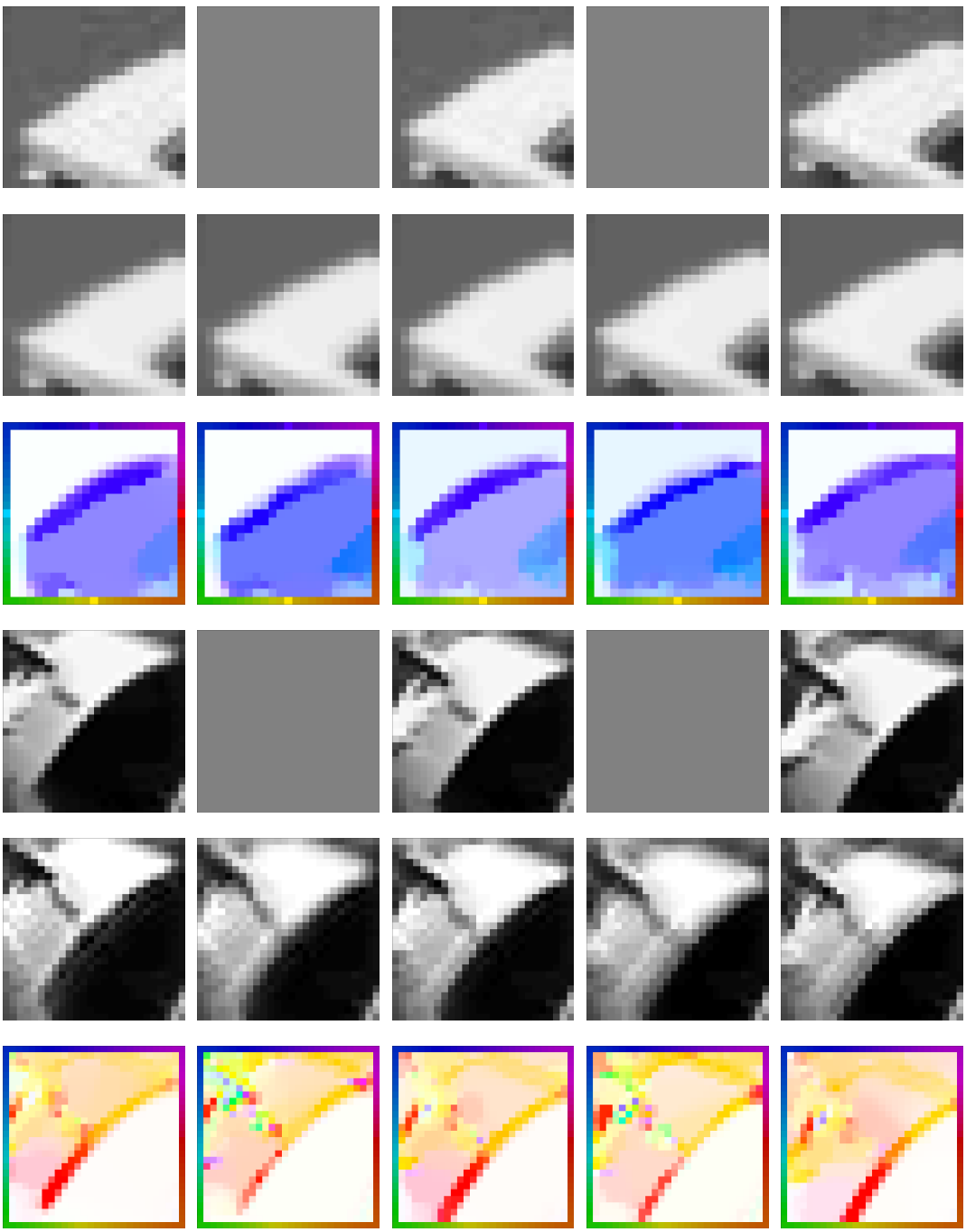

Figure 5. *Zoom into the Hamburg taxi (from Nagel) and Mini Cooper* [3] *sequences. First and fourth row: Input images, grey ones are unknown. Second and fifth row: Resulting sequence including time interpolants. Third and sixth row: Estimated flow fields. The full images can be found in Appendix* E *(Figures* 8 *and* 9*).*

Downloaded 07/11/18 to 131.111.184.102. Redistribution subject to SIAM license or copyright; see http://www.siam.org/journals/ojsa.php

Copyright © by SIAM. Unauthorized reproduction of this article is prohibited.

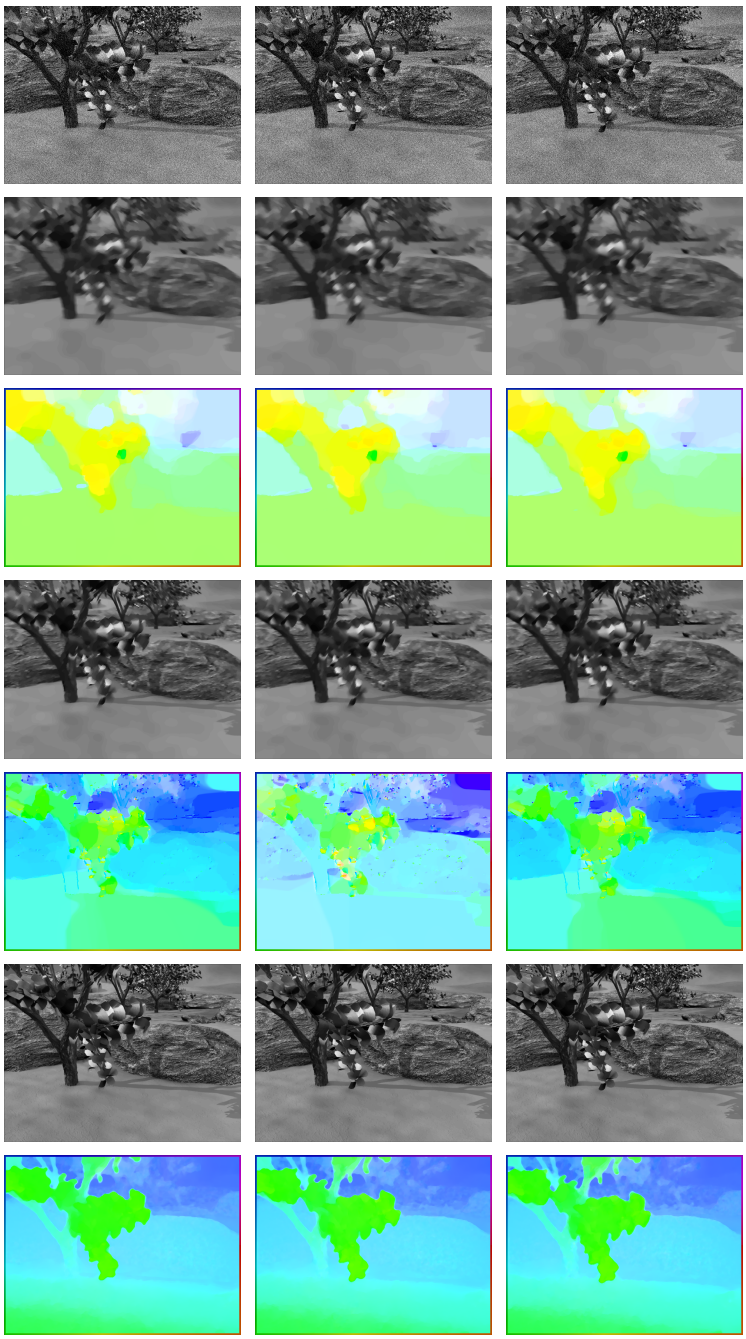

Figure 6. *First three frames from the large-scale motion experiment. First row contains input images, second and third row display the image reconstruction and motion estimation performed by the proposed model, rows four and five show the results using temporal interpolation, and the last two rows contain results generated by an improved model for large-scale motion* [20].

Downloaded 07/11/18 to 131.111.184.102. Redistribution subject to SIAM license or copyright; see http://www.siam.org/journals/ojsa.php

Copyright © by SIAM. Unauthorized reproduction of this article is prohibited.

Downloaded 07/11/18 to 131.111.184.102. Redistribution subject to SIAM license or copyright; see http://www.siam.org/journals/ojsa.php

6. Conclusion. In this paper we propose a joint model for motion estimation and image reconstruction. The model takes a sequence of noisy images as input and simultaneously removes noise while estimating the optical flow between consecutive frames. For the proposed model the existence of a minimizer is proven and we introduce a numerical scheme using an L^1 penalty term for the optical flow constraint aiming at solving the variational energy by alternately applying a primal-dual method to the problem for the image sequence u and the flow sequence $\boldsymbol{v}$. The L^1 penalty approach is justified both from the theoretical and numerical viewpoint. In the results part we show the benefits of our method in contrast to classical methods for separate image denoising or motion estimation. The presented numerical results include image denoising and temporal inpainting but note that the well-posedness analyzed in this paper holds for a general linear operator K and in particular can include image deblurring, image inpainting, or sampled Radon transform. Finally, we present a main drawback of our model, namely, its limitation to motion of small magnitude and give an outlook to a possible extension for large-scale motion fields.

Appendix A. Notations. Throughout this work $\Omega \subset \mathbb{R}^2$ is an image domain and $\Omega_T := \Omega \times [0,T]$ a space-time domain. Moreover, $\mathcal{D}'(\Omega_T)$ denotes the space of distributions on Ω_T. The gradient operator ∇ (and the associated divergence operator $\nabla\cdot$) only refers to the spatial dimensions, while time derivatives are explicitly denoted with subindex t.

The total variation of u is a seminorm in the space of functions with $\mathrm{BV}(\Omega)$:

$$BV(\Omega) := \left\{ u \in L^1(\Omega) : |u|_{BV} = \sup_{\phi \in C_0^\infty(\Omega;\mathbb{R}^N), \|\phi\|_\infty \le 1} \int_\Omega u \nabla \cdot \phi dx < \infty \right\}. \tag{A.1}$$

For a functional $J : \Omega \to \mathbb{R}$, the sublevel set is the set of all u for which the functional value lies below α:

$$\mathcal{S}_\alpha := \{ u \in \Omega : J(u) < \alpha \}. \tag{A.2}$$

Due to the fact that the image domain consists of time and space, suitable spaces including space and time are required for the analysis in this paper. The Bochner space

$$L^p(0,T;\mathcal{X}) := \left\{ u : u(\cdot,t) \in \mathcal{X} \ \ \forall t \in [0,T], \int_0^T \|u(\cdot,t)\|_{\mathcal{X}}^p \, dt < \infty \right\}$$

is a Banach space with norm

$$\|u\|_{L^p(0,T;\mathcal{X})} = \left(\int_0^T \|u(\cdot,t)\|_{\mathcal{X}}^p \, dt \right)^{\frac{1}{p}}.$$

A very useful result that will be used in our analysis is the Aubin–Lions lemma.

Lemma A.1 (Aubin–Lions). *Let $\mathcal{X}, \mathcal{Y}, \mathcal{Z}$ be Banach spaces with a compact embedding $\mathcal{X} \subset\subset \mathcal{Y}$ and a continuous embedding $\mathcal{Y} \hookrightarrow \mathcal{Z}$. Let u^n be a sequence of bounded functions in $L^p(0,T;\mathcal{X})$ and $\partial_t u^n$ be bounded in $L^q(0,T;\mathcal{Z})$ (for $q = 1$ and $1 \le p < \infty$ or $q > 1$ and $1 \le p \le \infty$).*

Then u^n is relatively compact in $L^p(0,T;\mathcal{Y})$.

Copyright © by SIAM. Unauthorized reproduction of this article is prohibited.

Proof. See [2, 27, 40] for the proof. ∎

In other words: If there exists a compact embedding from one space into another, the compact embedding carries over to the induced Bochner space if enough time regularity can be shown.

Appendix B. Error measures. To evaluate the performance of the overall model, quality measures for the reconstructed image sequence and the velocity field are needed.

To measure the quality of the reconstructed image sequence we consider the structural similarity index (*SSIM*) [46], which measures the difference in luminance, contrast, and structure of the ground-truth image u and the reconstruction u_{rec} as follows:

$$SSIM := \frac{(2\mu_u\mu_{u_{rec}} + C_1)(2\sigma_{u,u_{rec}} + C_2)}{(\mu_u^2 + \mu_{u_{rec}}^2 + C_1)(\sigma_u^2 + \sigma_{u_{rec}}^2 + C_2)},$$

where $\mu_u, \mu_{u_{rec}}, \sigma_u, \sigma_{u_{rec}}$, and $\sigma_{u,u_{rec}}$ are local means, standard deviations, and cross covariances for ground-truth image u and reconstruction u_{rec}, respectively. The constants are fixed to $C_1 = 0.01^2$ and $C_2 = 0.03^2$. The SSIM takes values between -1 and 1, where 1 stands for perfect similarity. Moreover, we calculate the **SNR** and **PSNR** between ground truth u and reconstruction u_{rec}:

$$SNR := 10\log_{10}\left(\frac{\text{mean}(u^2)}{\text{mean}((u-u_{rec})^2)}\right),$$
$$PSNR := 10\log_{10}\left(\frac{\max(u^2)}{\text{mean}((u-u_{rec})^2)}\right).$$

For the evaluation of the motion field we refer to the work of Baker et al. [3]. The most intuitive measure presented there is the average endpoint error **AEE** proposed in [30], which is the vector-wise Euclidean norm of the difference vector $\boldsymbol{v} - \boldsymbol{v}_{GT}$, where $\boldsymbol{v}$ is the reconstructed velocity field and $\boldsymbol{v}_{GT}$ is the true velocity field. For normalization, the difference is divided by $|\Omega|$ and we have

$$AEE := \frac{1}{|\Omega|}\int_\Omega \sqrt{(v_1(x) - v_1^{GT}(x))^2 + (v_2(x) - v_2^{GT}(x))^2}\mathrm{d}x. \tag{B.1}$$

Another measure we use is the angular error (AE), which goes back to the work of Fleet and Jepson [21] and a survey of Barron, Fleet, and Beauchemin [5]. Here $\boldsymbol{v}$ and $\boldsymbol{v}^{GT}$ are projected into the 3d space (to avoid division by zero) and normalized as follows:

$$\hat{\boldsymbol{v}} := \frac{(v_1, v_2, 1)}{\sqrt{\|\boldsymbol{v}\|^2 + 1}}, \qquad \hat{\boldsymbol{v}}^{GT} := \frac{(v_1^{GT}, v_2^{GT}, 1)}{\sqrt{\|\boldsymbol{v}^{GT}\|^2 + 1}}.$$

The error is then calculated measuring the angle between $\hat{\boldsymbol{v}}$ and $\hat{\boldsymbol{v}}_{GT}$ in the continuous setting as

$$AE := \frac{1}{|\Omega|}\int_\Omega \arccos(\hat{\boldsymbol{v}}(x) \cdot \hat{\boldsymbol{v}}_{GT}(x))\mathrm{d}x,$$

Copyright © by SIAM. Unauthorized reproduction of this article is prohibited.

Downloaded 07/11/18 to 131.111.184.102. Redistribution subject to SIAM license or copyright; see http://www.siam.org/journals/ojsa.php

Downloaded 07/11/18 to 131.111.184.102. Redistribution subject to SIAM license or copyright; see http://www.siam.org/journals/ojsa.php

Appendix C. ADMM Scheme. In this section we present an alternative to the primal-dual iterative scheme from section 4 which is based on an augmented Lagrangian approach. For the constrained problem,

$$\begin{aligned}&\arg\min_{u,\boldsymbol{v}} \int_0^T \frac{1}{2}\|Ku-f\|_2^2 + \alpha\|\nabla u\|_{2,1} + \beta\left(\|\nabla v_1\|_{2,1} + \|\nabla v_2\|_{2,1}\right)\mathrm{d}t,\\ &\text{s.t. } u_t + \nabla u\cdot\boldsymbol{v} = 0;\end{aligned}$$

the augmented Lagrangian formulation reads

$$\begin{aligned}\mathcal{L}(u,\boldsymbol{v},\lambda) = \int_0^T &\frac{1}{2}\|Ku-f\|_2^2 + \alpha\|\nabla u\|_{2,1} + \beta\left(\|\nabla v_1\|_{2,1} + \|\nabla v_2\|_{2,1}\right)\\ &+ \langle\lambda, u_t + \nabla u\cdot\boldsymbol{v}\rangle + \frac{\mu}{2}\|u_t + \nabla u\cdot\boldsymbol{v}\|_2^2\mathrm{d}t.\end{aligned}$$

The method of multipliers then alternatingly iterates between a minimization problem for $(u,\boldsymbol{v})$ and a subsequent gradient ascent for the Lagrange multiplier λ that reads as follows:

$$\begin{aligned}\left(u^{k+1},\boldsymbol{v}^{k+1}\right) = \arg\min_{u,\boldsymbol{v}} &\int_0^T \frac{1}{2}\|Ku-f\|_2^2 + \alpha\|\nabla u\|_{2,1} + \beta\left(\|\nabla v_1\|_{2,1} + \|\nabla v_2\|_{2,1}\right)\\ &+ \left\langle\lambda^k, u_t + \nabla u\cdot\boldsymbol{v}\right\rangle + \frac{\mu}{2}\|u_t + \nabla u\cdot\boldsymbol{v}\|_2^2\mathrm{d}t,\end{aligned} \tag{C.1}$$

$$\lambda^{k+1} = \lambda^k + \mu\left(u_t^{k+1} + \nabla u^{k+1}\cdot\boldsymbol{v}^{k+1}\right). \tag{C.2}$$

Problem (C.1) is very similar to our proposed unconstrained L^1 minimization formulation (see (4.1)) with the difference that the optical flow is penalized in the squared L^2 norm instead of the L^1 norm and an additional inner product occurs. From the numerical viewpoint the problem is challenging in the same way due to the nonlinearity of the optical flow formulation. Similarly to our approach, one could alternately fix u, respectively, $\boldsymbol{v}$ and optimize for the other variable, but convergence cannot be guaranteed for this scheme either.

A drawback in terms of runtime originates from the iteration between (C.1) and (C.2), because the full nonlinear problem has to be solved for each iteration.

We have implemented the augmented Lagrangian method for this problem using FlexBox [19] and alternately minimize with respect to u and v and afterwards update λ. The result can be found in Figure 7. We can see minor differences compared to the proposed L^1 penalty approach. From a visual point of view, both reconstructions are good and they are hard to differentiate. For the velocity field, the L^1 penalty contains sharper edges, while the augmented Lagrangian contains smoother transitions in the flow field. The L^1 penalty method has an AEE of 0.069 for the Grove 2 sequence and an AEE of 0.061 for the rubber whale sequence. The augmented Lagrangian method results for the Grove 2 sequence in a slightly better AEE of 0.64, but has a worse AEE of 0.68 for rubber whale.

In general, the augmented Lagrangian method does not allow any violation of the optical flow constraint and results in visually smoother results. The penalty approach on the other hand allows for outliers and therefore the flow field contains small artifacts where the violation

Copyright © by SIAM. Unauthorized reproduction of this article is prohibited.

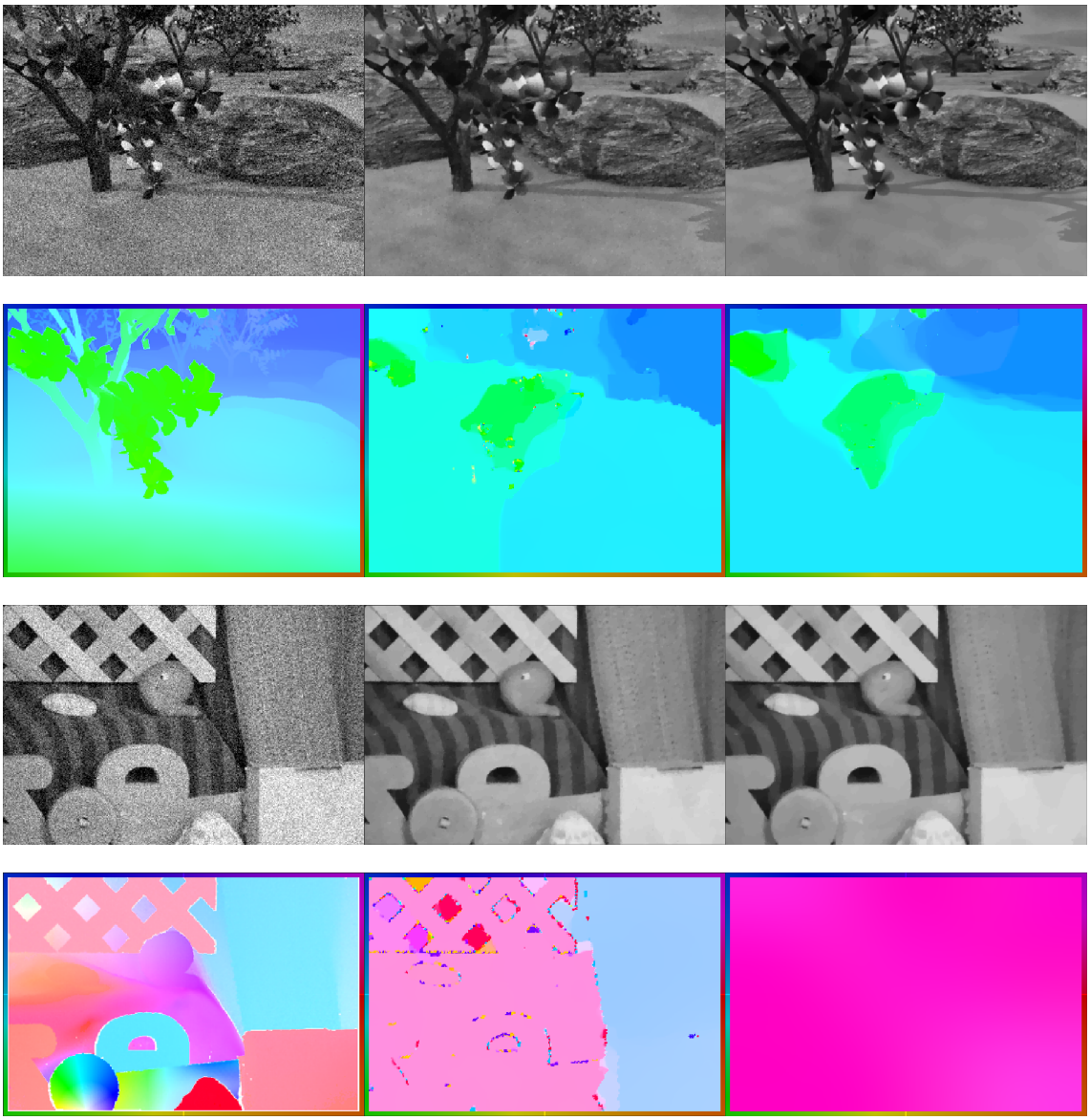

Figure 7. *Comparison of L^1 penalty term for the optical flow constraint versus augmented Lagrangian, where parameters are the same as in section 5.2. The top and third rows show the second frame of the noisy input data, the L^1 penalty reconstruction, and the augmented Lagrangian reconstruction. The second and fourth rows show the ground-truth motion field, and the estimated motion fields with L^1 penalty reconstruction and augmented Lagrangian reconstruction, respectively.*

of the optical flow constraint is beneficial for the total energy. Both methods will most likely converge to local minima due the nonlinearity of the problem, but it is unclear if one strategy is preferable in general. An extended comparison of both methods (and other minimization approaches) is beyond the scope of this paper.

Copyright © by SIAM. Unauthorized reproduction of this article is prohibited.

Downloaded 07/11/18 to 131.111.184.102. Redistribution subject to SIAM license or copyright; see http://www.siam.org/journals/ojsa.php

Downloaded 07/11/18 to 131.111.184.102. Redistribution subject to SIAM license or copyright; see http://www.siam.org/journals/ojsa.php

Appendix D. Discretization. First, we assume the underlying space-time grid to consist of the following set of discrete points:

$$\{(i,j,t) : i = 1,\dots,n_x, j = 1,\dots,n_y, t = 1,\dots,n_t\}.$$

Therefore, the image u and each of the vector components v_1 and v_2 are quantities in $X = \mathbb{R}^{n_x n_y n_t}$, whereas the (spatial) gradient is a vector in the space $Y = X \times X$. The spaces X and Y are equipped with standard scalar products. The resulting discrete derivatives for v_i are calculated using forward differences and Neumann boundary conditions. The corresponding adjoint operator consists of backward differences with Dirichlet boundary conditions and is applied to the dual variables $\boldsymbol{y}$. The resulting scheme reads

$$v_x^i(i,j) = \begin{cases} v(i+1,j) - v(i,j) & \text{if } i < n_x, \\ 0 & \text{if } i = n_x, \end{cases}$$

$$v_y^i(i,j) = \begin{cases} v(i,j+1) - v(i,j) & \text{if } j < n_y, \\ 0 & \text{if } j = n_y, \end{cases}$$

$$\nabla \cdot \boldsymbol{y}(i,j), = \begin{cases} y_1(i,j) - y_1(i-1,j) & \text{if } i > 1, \\ y_1(i,j) & \text{if } i = 1, \\ -y_1(i-1,j) & \text{if } i = n_x, \end{cases}$$

$$+ \begin{cases} y_2(i,j) - y_2(i,j-1) & \text{if } j > 1, \\ y_2(i,j) & \text{if } j = 1, \\ -y_2(i,j-1) & \text{if } j = n_y. \end{cases}$$

The discrete derivatives for the regularizer of u have the same structure. For the operator in the optical flow part we use a forward discretization for the temporal derivative and a central discretization for the spatial derivative. Again, Neumann boundary conditions are applied:

$$u_t(i,j,t) = \begin{cases} u(i,j,t+1) - u(i,j,t) & \text{if } t < n_t, \\ 0 & \text{else}, \end{cases}$$

$$u_x(i,j,t) = \begin{cases} \frac{u(i+1,j,t) - u(i-1,j,t)}{2} & \text{if } i > 1 \text{ and } i < n_x \text{ and } t < n_t, \\ 0 & \text{else}, \end{cases}$$

$$u_y(i,j,t) = \begin{cases} \frac{u(i,j+1,t) - u(i,j-1,t)}{2} & \text{if } j > 1 \text{ and } j < n_y \text{ and } t < n_t, \\ 0 & \text{else}. \end{cases}$$

Copyright © by SIAM. Unauthorized reproduction of this article is prohibited.

Downloaded 07/11/18 to 131.111.184.102. Redistribution subject to SIAM license or copyright; see http://www.siam.org/journals/ojsa.php

The adjoint operator then yields:

$$y_t(i,j,t) = \begin{cases} y(i,j,t) - y(i,j,t-1) & \text{if } t > 1 \text{ and } t < n_t, \\ y(i,j,t) & \text{if } t = 1, \\ -y(i,j,t-1) & \text{if } t = n_t, \end{cases}$$

$$y_x(i,j,t) = \begin{cases} \frac{y(i+1,j,t)-y(i-1,j,t)}{2} & \text{if } i > 1 \text{ and } i < n_x - 1 \text{ and } t < n_t, \\ \frac{y(i+1,j,t)}{2} & \text{if } i \leq 1 \text{ and } t < n_t, \\ \frac{y(i-1,j,t)}{2} & \text{if } i \geq n_x - 1 \text{ and } t < n_t, \\ 0 & \text{else}, \end{cases}$$

$$y_y(i,j,t) = \begin{cases} \frac{y(i,j+1,t)-y(i,j-1,t)}{2} & \text{if } j > 1 \text{ and } j < n_y - 1 \text{ and } t < n_t, \\ \frac{y(i,j+1,t)}{2} & \text{if } j \leq 1 \text{ and } t < n_t, \\ \frac{y(i,j-1,t)}{2} & \text{if } j \geq n_y - 1 \text{ and } t < n_t, \\ 0 & \text{else.} \end{cases}$$

The symbol $\|\nabla u\|_{2,1}$ represents the discrete spatial isotropic TV

$$\|\nabla u\|_{2,1} := \sum_{i,j,t} \left| \sqrt{u_x(i,j,t)^2 + u_y(i,j,t)^2} \right|.$$

In analogy we define $\|y\|_{2,\infty}$ for a vectorial quantity $y = (y_1, y_2)$ as

$$\|y\|_{2,\infty} := \max_{i,j,t} \sqrt{y_1(i,j,t)^2 + y_2(i,j,t)^2}.$$

The primal-dual formulation of the underlying problems contains several indicator functions on convex sets denoted as

$$\delta_Y(\tilde{y}) := \begin{cases} 0 & \text{if } \tilde{y} \in Y, \\ \infty & \text{else.} \end{cases}$$

For a functional $J(x) = \|x\|_{2,1}$, where $x = (x_1, x_2)$ represents a vectorial quantity on the previously defined grid, we calculate the convex conjugate $J^*(p)$ as

$$\begin{aligned} J^*(p) &= \sup_x \langle p, x \rangle - J(x) = \sup_x \langle p, x \rangle - \|x\|_{2,1} \\ &= \sup_x \sum_{i,j,t} p_1(i,j,t)x_1(i,j,t) + p_2(i,j,t)x_2(i,j,t) - \sqrt{x_1(i,j,t)^2 + x_2(i,j,t)^2}. \end{aligned}$$

At this point the argumentation can be done for each summand independently and we see that if $\sqrt{p_1(i,j,t)^2 + p_2(i,j,t)^2} > 1$ for any (i,j,t) the supremum takes infinity. If on the other hand $\sqrt{p_1(i,j,t)^2 + p_2(i,j,t)^2} \leq 1$ the supremum takes 0. Consequently, we calculate

$$J^*(p) = \begin{cases} 0 & \text{if } \max_{i,j,t} \sqrt{p_1(i,j,t)^2 + p_2(i,j,t)^2} \leq 1, \\ \infty & \text{else,} \end{cases}$$

Copyright © by SIAM. Unauthorized reproduction of this article is prohibited.

as the convex conjugate for the isotropic total variation. For $J(x) = \frac{1}{2}\|x\|_2^2$ one can easily calculate the convex conjugate as $J^*(p) = \frac{1}{2}\|p\|_2^2$.

Let us furthermore recall some basic rules for the convex conjugates:

$$\begin{aligned}(J(\cdot + a))^* &= J^*(\cdot) - \langle \cdot, a \rangle, \\ (J(\cdot) + a)^* &= J^*(\cdot) - a, \\ (\lambda J(\cdot))^* &= \lambda J^*\left(\frac{\cdot}{\lambda}\right), \quad \lambda > 0.\end{aligned}$$

Appendix E. Algorithm.

Algorithm 1 Joint *TV-TV* Optical Flow Motion Estimation and Image Reconstruction.

function JointTVTVOpticalFlow$(f, \alpha, \beta, \gamma, K)$
  $v, u \leftarrow 0$
  while $\epsilon < threshold$ **do**
    $u_{OldM} \leftarrow u$
    $\boldsymbol{v}_{OldM} \leftarrow \boldsymbol{v}$
    $y, \bar{u} \leftarrow 0$
    while $\epsilon_u < threshold$ **do**
      $u_{Old} \leftarrow u$
      $\tilde{\boldsymbol{y}} \leftarrow \boldsymbol{y} + \sigma C_u \bar{u}$
      $y_1 \leftarrow \frac{\tilde{y_1} - \sigma f}{\sigma + 1}$
      $y_2 \leftarrow \pi_\alpha(\tilde{y_2})$
      $y_3 \leftarrow \pi_\gamma(\tilde{y_3})$
      $u \leftarrow u - \tau C_u^T \boldsymbol{y}$
      $\bar{u} \leftarrow 2u - u_{Old}$
    end while
    $y, \bar{\boldsymbol{v}} \leftarrow 0$
    while $\epsilon_v < threshold$ **do**
      $\boldsymbol{v}_{Old} \leftarrow \boldsymbol{v}$
      $\tilde{\boldsymbol{y}} \leftarrow \boldsymbol{y} + \sigma C_v \bar{\boldsymbol{v}}$
      $\boldsymbol{y} \leftarrow \pi_\lambda(\tilde{\boldsymbol{y}})$
      $\tilde{\boldsymbol{v}} \leftarrow \boldsymbol{v} - \tau C_v^T \boldsymbol{y}$
      $\boldsymbol{v} \leftarrow solveAffine(\tilde{\boldsymbol{v}})$
      $\bar{\boldsymbol{v}} \leftarrow 2\boldsymbol{v} - \boldsymbol{v}_{Old}$
    end while
    $\epsilon \leftarrow \frac{|u - u_{OldM}| + |\boldsymbol{v} - \boldsymbol{v}_{OldM}|}{2|\Omega|}$
  end while
  return v
end function

Full resolution of the Hamburg taxi and Mini Cooper sequences are given in Figures 8 and 9.

Copyright © by SIAM. Unauthorized reproduction of this article is prohibited.

Downloaded 07/11/18 to 131.111.184.102. Redistribution subject to SIAM license or copyright; see http://www.siam.org/journals/ojsa.php

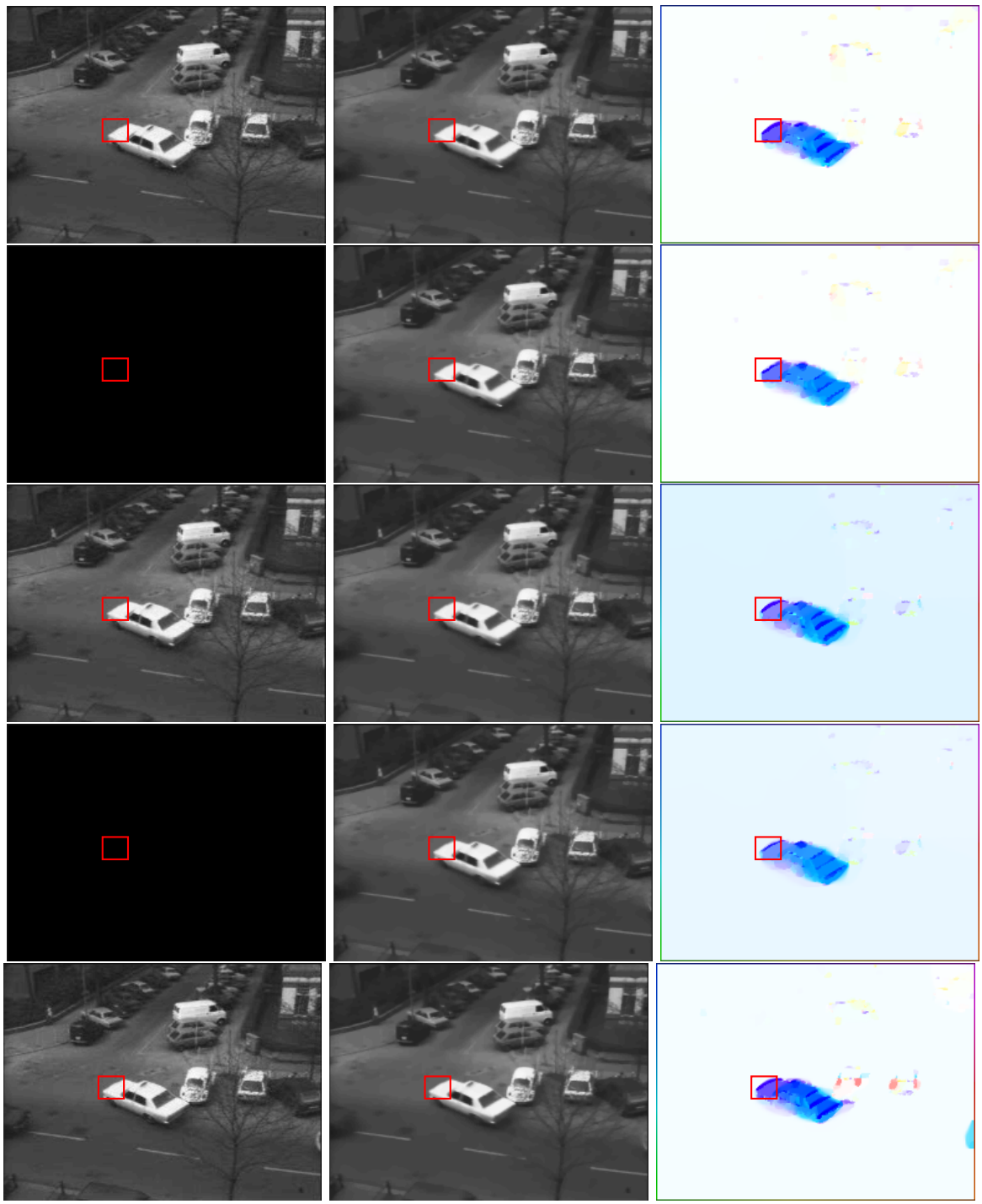

Figure 8. *Full resolution Hamburg taxi sequence (from Nagel). Left: Input images, black are unknown. Middle: Resulting sequence including time interpolants.*

Downloaded 07/11/18 to 131.111.184.102. Redistribution subject to SIAM license or copyright; see http://www.siam.org/journals/ojsa.php

Copyright © by SIAM. Unauthorized reproduction of this article is prohibited.

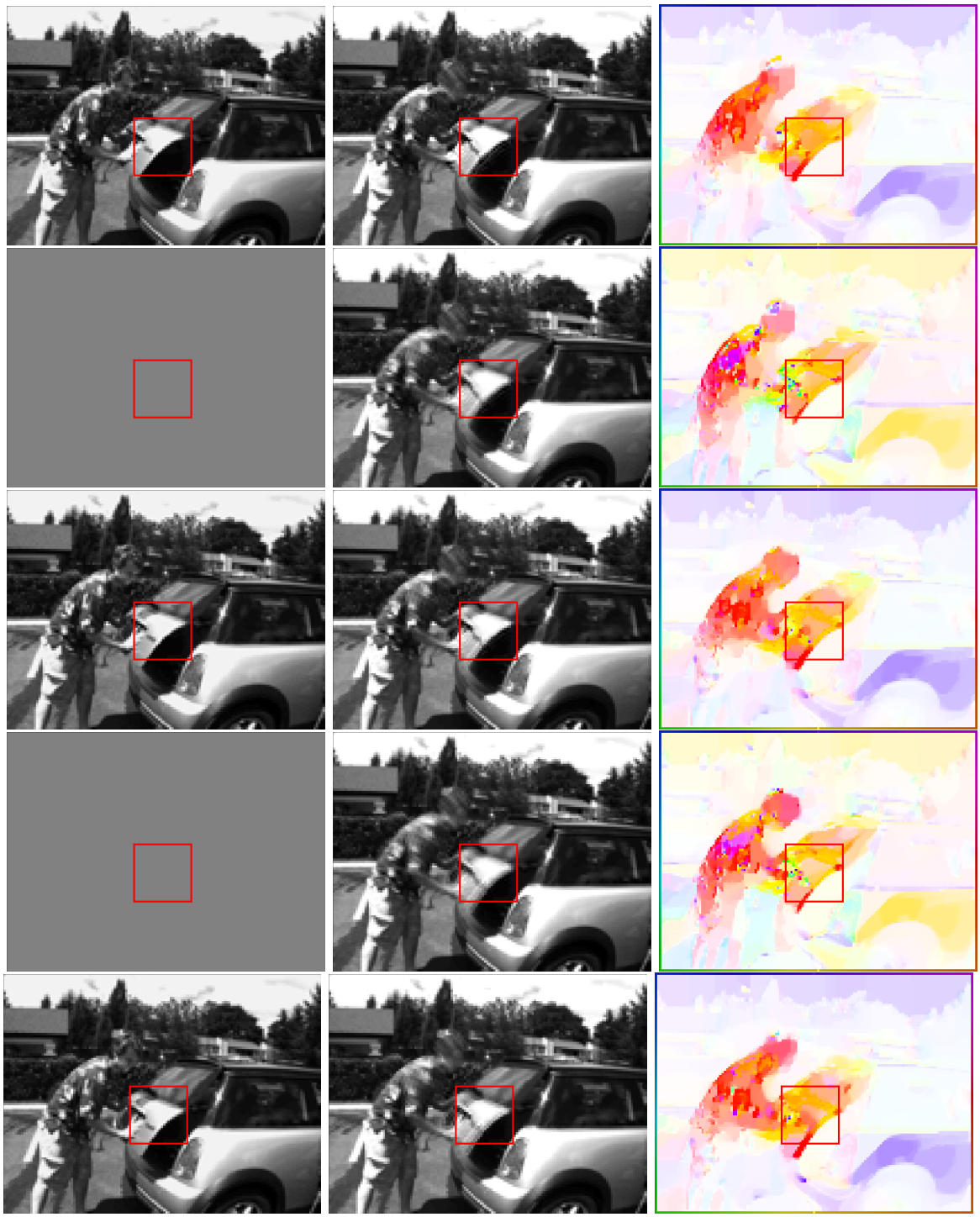

Figure 9. *Full resolution Mini Cooper sequence (Middlebury). Left: Input images, grey are unknown. Middle: Resulting sequence including time interpolants. Right: Estimated flow fields.*

Downloaded 07/11/18 to 131.111.184.102. Redistribution subject to SIAM license or copyright; see http://www.siam.org/journals/ojsa.php

Copyright © by SIAM. Unauthorized reproduction of this article is prohibited.

REFERENCES

[1] G. Aubert, R. Deriche, and P. Kornprobst, *Computing optical flow via variational techniques*, SIAM J. Appl. Math., 60 (1999), pp. 156–182.

[2] J.-P. Aubin, *Un théorème de compacité*, C. R. Acad. Sci. Paris, 256 (1963), pp. 5042–5044.

[3] S. Baker, D. Scharstein, J. P. Lewis, S. Roth, M. J. Black, and R. Szeliski, *A database and evaluation methodology for optical flow*, Int. J. Comput. Vis., 92 (2011), pp. 1–31.

[4] L. Bar, B. Berkels, M. Rumpf, and G. Sapiro, *A variational framework for simultaneous motion estimation and restoration of motion-blurred video*, in Proceedings of the IEEE 11th International Conference on Computer Vision, 2007, ICCV 2007, IEEE, Piscataway, NJ, 2007, 4409009.

[5] J. L. Barron, D. J. Fleet, and S. S. Beauchemin, *Performance of optical flow techniques*, Int. J. Comput. Vis., 12 (1994), pp. 43–77.

[6] J.-D. Benamou and Y. Brenier, *A computational fluid mechanics solution to the Monge-Kantorovich mass transfer problem*, Numer. Math. 84 (2000), pp. 375–393.

[7] J.-D. Benamou, Y. Brenier, and K. Guittet, *The Monge–Kantorovitch mass transfer and its computational fluid mechanics formulation*, Int. J. Numer. Methods Fluids, 40 (2002), pp. 21–30.

[8] J.-D. Benamou, G. Carlier, and F. Santambrogio, *Variational mean field games*, in Active Particles, Vol. 1, Birkhäuser, Cham, Switzerland, 2017, pp. 141–171.

[9] M. Benning, C. Brune, M. Burger, and J. Müller, *Higher-order TV methods-enhancement via Bregman iteration*, J. Sci. Comput., 54 (2013), pp. 269–310.

[10] A. Borzi, K. Ito, and K. Kunisch, *Optimal control formulation for determining optical flow*, SIAM J. Sci. Comput., 24 (2003), pp. 818–847.

[11] K. Bredies and M. Holler, *Regularization of linear inverse problems with total generalized variation*, J. Inverse Ill-Posed Probl., 22 (2014), pp. 871–913.

[12] K. Bredies, K. Kunisch, and T. Pock, *Total generalized variation*, SIAM J. Imaging Sci., 3 (2010), pp. 492–526.

[13] C. Brune, *4D Imaging in Tomography and Optical Nanoscopy*, Ph.D. thesis, University of Münster, Münster, Germany, 2010.

[14] M. Burger, A. C. G. Mennucci, S. Osher, and M. Rumpf, *Level Set and PDE Based Reconstruction Methods in Imaging*, Springer, Cham, Switzerland, 2013.

[15] M. Burger, J. Modersitzki, and S. Suhr, *A Nonlinear Variational Approach to Motion-Corrected Reconstruction of Density Images*, preprint, http://arxiv.org/abs/1511.09048 (2015).

[16] B. Cengiz, *The dual of the Bochner space $L^p(\mu, E)$ for arbitrary μ*, Turkish J. Math., 22 (1998), pp. 343–348.

[17] A. Chambolle and T. Pock, *A first-order primal-dual algorithm for convex problems with applications to imaging*, J. Math. Imaging Vision, 40 (2011), pp. 120–145.

[18] H. Dirks, *Variational Methods for Joint Motion Estimation and Image Reconstruction*, Ph.D. thesis, WWU Münster, Münster, Germany, 2015.

[19] H. Dirks, *A Flexible Primal-Dual Toolbox*, preprint, arXiv:1603.05835, 2016.

[20] H. Dirks, *Joint Large-Scale Motion Estimation and Image Reconstruction*, preprint, http://arxiv.org/abs/1610.09908 (2016).

[21] D. J. Fleet and A. D. Jepson, *Computation of component image velocity from local phase information*, Int. J. Comput. Vis., 5 (1990), pp. 77–104.

[22] D. R. Gilland, B. A. Mair, J. E. Bowsher, and R. J. Jaszczak, *Simultaneous reconstruction and motion estimation for gated cardiac ect*, IEEE Trans. Nucl. Sci., 49 (2002), pp. 2344–2349.

[23] T. Goldstein, E. Esser, and R. Baraniuk, *Adaptive Primal-Dual Hybrid Gradient Methods for Saddle-Point Problems*, preprint, http://arxiv.org/abs/1305.0546 (2013).

[24] T. Goldstein and S. Osher, *The split Bregman method for l1-regularized problems*, SIAM J. Imaging Sci., 2 (2009), pp. 323–343.

[25] B. K. Horn and B. G. Schunck, *Determining optical flow*, Artif. Intell., 17 (1981), pp. 185–203.

[26] T. Kösters, K. P. Schäfers, and F. Wübbeling, *Emrecon: An expectation maximization based image reconstruction framework for emission tomography data*, in Proceedings of the Nuclear Science Symposium and Medical Imaging Conference (NSS/MIC), 2011 IEEE, Piscataway, NJ, 2011, pp. 4365–4368.

Downloaded 07/11/18 to 131.111.184.102. Redistribution subject to SIAM license or copyright; see http://www.siam.org/journals/ojsa.php

Copyright © by SIAM. Unauthorized reproduction of this article is prohibited.

[27] J.-L. Lions, *Quelques Méthodes de Résolution des Problèmes aux Limites Non Linéaires*, Dunod, Paris, 1969.
[28] N. G. Meyers and W. P. Ziemer, *Integral inequalities of Poincaré and Wirtinger type for BV functions*, Amer. J. Math., (1977), pp. 1345–1360.
[29] D. Mitzel, T. Pock, T. Schoenemann, and D. Cremers, *Video Super Resolution using Duality Based TV-L1 Optical Flow*, in Pattern Recognition, Springer, Berlin, 2009, pp. 432–441.
[30] M. Otte and H.-H. Nagel, *Optical flow estimation: Advances and comparisons*, in Computer Vision–ECCV'94, Springer, New York, 1994, pp. 49–60.
[31] N. Papenberg, A. Bruhn, T. Brox, S. Didas, and J. Weickert, *Highly accurate optic flow computation with theoretically justified warping*, Int. J. Comput. Vis., 67 (2006), pp. 141–158.
[32] N. Parikh and S. P. Boyd, *Proximal algorithms*, Found. Trends Optim., 1 (2014), pp. 127–239.
[33] T. Pock, D. Cremers, H. Bischof, and A. Chambolle, *An algorithm for minimizing the Mumford-Shah functional*, in Proceedings of the 2009 IEEE 12th International Conference on Computer Vision, IEEE, Piscataway, NJ, 2009, pp. 1133–1140.
[34] L. I. Rudin, S. Osher, and E. Fatemi, *Nonlinear total variation based noise removal algorithms*, Phys. D, 60 (1992), pp. 259–268.
[35] W. Rudin, *Functional Analysis*, McGraw-Hill, New York, 1973.
[36] A. Sawatzky, C. Brune, F. Wubbeling, T. Kosters, K. Schafers, and M. Burger, *Accurate EM-TV algorithm in PET with low SNR*, in Proceedings of the 2008 IEEE Nuclear Science Symposium Conference Record, IEEE, Piscataway, NJ, 2008, pp. 5133–5137.
[37] H. Schaeffer, Y. Yang, and S. Osher, *Real-Time Adaptive Video Compressive Sensing*, Technical report, UCLA CAM, UCLA, Los Angeles, 2013.
[38] H. Shen, L. Zhang, B. Huang, and P. Li, *A map approach for joint motion estimation, segmentation, and super resolution*, IEEE Trans. Image Process., 16 (2007), pp. 479–490.
[39] J. Shen and T. F. Chan, *Mathematical models for local nontexture inpaintings*, SIAM J. Appl. Math., 62 (2002), pp. 1019–1043.
[40] J. Simon, *Compact sets in the space $L^p(0,T;B)$*, Ann. Mat. Pura Appl. (4), 146 (1986), pp. 65–96.
[41] L. Tartar, *The compensated compactness method applied to systems of conservation laws*, in Systems of Nonlinear Partial Differential Equations, Springer, Dordrecht, The Netherlands, 1983, pp. 263–285.
[42] C. Tomasi and T. Kanade, *Shape and motion from image streams under orthography: A factorization method*, Int. J. Comput. Vis., 9 (1992), pp. 137–154.
[43] M. Unger, T. Pock, M. Werlberger, and H. Bischof, *A convex approach for variational super-resolution*, in Pattern Recognition, Springer, Berlin, 2010, pp. 313–322.
[44] S. Volz, A. Bruhn, L. Valgaerts, and H. Zimmer, *Modeling temporal coherence for optical flow*, in Proceedings of 2011 International Conference on Computer Vision, IEEE, Piscataway, NJ, 2011, pp. 1116–1123.
[45] Y. Wang, W. Yin, and Y. Zhang, *A Fast Algorithm for Image Deblurring with Total Variation Regularization*, Technical report, CAAM TR07-10, Rice University, Houston, TX, 2007.
[46] Z. Wang, A. C. Bovik, H. R. Sheikh, and E. P. Simoncelli, *Image quality assessment: From error visibility to structural similarity*, IEEE Trans. Image Process., 13 (2004), pp. 600–612.
[47] C. Zach, T. Pock, and H. Bischof, *A duality based approach for realtime TV-L1 optical flow*, in Pattern Recognition, Springer, Berlin, 2007, pp. 214–223.

Downloaded 07/11/18 to 131.111.184.102. Redistribution subject to SIAM license or copyright; see http://www.siam.org/journals/ojsa.php

Copyright © by SIAM. Unauthorized reproduction of this article is prohibited.